Industrial Crops & Products 186 (2022) 115247

Contents lists available at ScienceDirect

Industrial Crops & Products

journal homepage: www.elsevier.com/locate/indcrop

Micro and nanocellulose extracted from energy crops as reinforcement agents in chitosan films

João R.A. Pires [a], Victor G.L. Souza [a,b], Leandro A. Gomes [a], Isabel M. Coelhoso [c], Maria H. Godinho [d], Ana L. Fernando [a,*]

[a] MEtRICs, Departamento de Ciências e Tecnologia da Biomassa/Departamento de Química, NOVA School of Science and Technology=FCT NOVA, Universidade Nova de Lisboa, Campus de Caparica, 2829-516 Caparica, Portugal
[b] INL, International Iberian Nanotechnology Laboratory, Av. Mestre José Veiga s/n, 4715-330 Braga, Portugal
[c] LAQV-REQUIMTE, Departamento de Química, NOVA School of Science and Technology=FCT NOVA, Universidade Nova de Lisboa, Campus de Caparica, 2829-516 Caparica, Portugal
[d] CENIMAT=I3N, Departamento de Ciências dos Materiais, NOVA School of Science and Technology=FCT NOVA, Universidade Nova de Lisboa, Campus de Caparica, 2829-516 Caparica, Portugal

ARTICLE INFO

Keywords:
Biocomposites
Energy Crops
Giant reed
Kenaf
Miscanthus
Nanocrystalline cellulose

ABSTRACT

The quest for more renewable and biodegradable materials currently represents a scientific key focus to combat the massive maneuver of non-sustainable products. Lignocellulosic feedstocks are rich in cellulose, hemicellulose, and lignin which, when recovered and separated, can give rise to innovative value-added products. Cellulose at the micro (MCC) and nanosized crystalline particles (CNC) are suitable examples of bioproducts that provide applications in many distinctive areas. The insertion of these homogeneously scattered particles, as a reinforcement agent, into the chitosan (Ch) films, is seen as a promising possibility to surpass the shortcomings associated with bioplastics. Therefore, the aim of this work was to test a combination of MCC and CNC obtained from biomass from giant reed (*Arundo donax* L.), kenaf (*Hibiscus cannabinus* L.) and, miscanthus (*Miscanthus* × *giganteus* Greef et Deu.) as reinforcement agents in Ch films. Extraction of MCC and CNC was carried out via an alkaline pre-treatment approach followed by acid hydrolysis. The particles were incorporated in Ch at different rates (1.5 %, 2 %, and 2.5 % w/w of chitosan), and the resultant biocomposites were fully characterized in terms of their morphology, mechanical and optical properties, permeability (oxygen and water vapor), water wettability, thermal analysis, X-ray diffraction, and FT-IR. Chitosan films reinforced with commercial nanocellulose at the same rates were tested for comparison. It was observed an improvement for the majority of samples after the incorporation of MCC/CNC, as planned. The sample with MCC/CNC isolated from giant reed was the one that most improved the properties of the film. Between the amounts added, the 2.5 % level presented the most encouraging effects, by improving considerably the strength and stiffness and by reducing the oxygen and water vapor permeabilities, essential features in the use of bio-based films by e.g. the food packaging industry. For this MCC/CNC rate, the films demonstrated equivalent potential to the film with 2 % commercial CNC. Predominantly, the different analyses displayed in the study indicated that biomass from the three lignocellulosic crops tested may afford a viable alternative source of reinforcing agents to be applied in the biocomposites production.

1. Introduction

The excellent structural properties associated with fossil-based plastics highlight them as an indispensable material that serves as a packaging foundation for several daily life products. However, the non-degradability and abusive handling have turned it into an acute universal dilemma that should be addressed. The most accurate attitude that people, as consumers, should adopt to overcome this challenging situation is to pursue the rule of the three Rs (reduce, reuse, and recycle) (Emadian et al., 2017; Pires et al., 2022a, 2022b; Thakur et al., 2018). Therefore, it is noteworthy to explore the development of biodegradable materials that may replace traditional plastics, especially in places with

* Corresponding author.
E-mail addresses: jr.pires@campus.fct.unl.pt (J.R.A. Pires), victor.souza@inl.int (V.G.L. Souza), lau.gomes@campus.fct.unl.pt (L.A. Gomes), imrc@fct.unl.pt (I.M. Coelhoso), mhg@fct.unl.pt (M.H. Godinho), ala@fct.unl.pt (A.L. Fernando).

https://doi.org/10.1016/j.indcrop.2022.115247
Received 18 February 2022; Received in revised form 9 June 2022; Accepted 16 June 2022
Available online 2 July 2022

more significant rates of waste disposal (Pires et al., 2019a, 2019b), through the reuse of wastes/byproducts of bio-based sources. In this way, there will be a contribution to the circular economy, and the materials being produced are biodegradable and renewable.

The bio-based plastics/polymers, recurrently expressed in literature as bioplastics/biopolymers, have been appointed recently as one attractive solution to replace petroleum-based plastics. These are extracted from renewable resources and can be found in nature with abundance at accessible prices. Moreover, they present good biodegradation and composting rates and own reduced or non-toxicity (Souza and Fernando, 2016). Production of novel biomaterials from waste or underutilized agro-food residues represents an appealing idea to fulfill that. In addition to the reuse of wasted resources, this approach is expectable to accomplish a reduction in processing costs (Brigham, 2018; Karan et al., 2019).

Chitosan is a polysaccharide obtained from the full or partial N-deacetylation of chitin, abundantly found in nature in the exoskeleton of marine arthropods (crustaceans) and in insects or in the cell walls of some specific *fungi* and *algae*. In the past decades, chitosan has been extensively studied due to its beneficial properties inherently associated with the available functional groups present in the chemical composition that enable the interaction with other active molecules (Alves et al., 2018; Noshirvani et al., 2017). The well-ordered hydrogen-bonded network configuration confers to chitosan films/coatings an effective barrier to gas transference, like O_2 and CO_2. On the opposing side, they typically own a hydrophilic nature resulting in poor water vapor and moisture barrier properties, which can represent an issue when applied in the production of composites for food packaging (Pires et al., 2018; Souza et al., 2017).

Combining the chitosan's good features with the advantageous gel-forming attribute and the native antimicrobial/antioxidant activity it will be possible to unlock access to functional active bio-based films and coatings on valuable scientific and technological markets like pharmaceutical, biomedical, agricultural, as well as food applications (Kumar et al., 2020). Nonetheless, with industry in mind, bioplastics made from polysaccharides still are structurally some points behind conventional plastics, demonstrating that it is needed optimizations mainly in terms of mechanical, thermal, and processing properties (Shankar and Rhim, 2018). Accordingly, to make it possible for a biopolymer-based film to pass from concept to reality, it is fundamental to strengthen its composition, modifying and improving its properties. The insertion of homogeneously dispersed micro/nanoparticles into the biopolymer matrix, with a high aspect ratio and high surface area, is seen as a promising solution, creating a novel functional class of materials named biocomposites (Fortunati et al., 2018). By definition, biocomposites consist of mixtures of a certain polymer (or biopolymer) reinforced with small quantities of inorganic or organic (or bio-based organic) fillers with a particular size, geometry, and surface chemistry (Bharimalla et al., 2017).

Cellulose is the most plentiful and renewable organic substance existent in the ecosystem, and its conversion to micro/nanosized particles (classified depending on the length and thickness of the particles) has been attracted the attention of biorefineries. Microcellulose can be characterized by spherical or rod-like particles with sizes of 10–200 μm, while the dimensions of CNCs can vary broadly, with diameter in the range of 5–50 nm and length in the range of 100–500 nm. Nanocellulose has been distinguished as a noteworthy biodegradable plant-based nanofiller, because of its unique optical, rheological, chemical structure (abundant hydroxyl groups), and mechanical properties (high strength and high specific surface area) even at low concentration (Chakrabarty and Teramoto, 2018; Chen et al., 2019; Gray, 2020; Kargarzadeh et al., 2017; Xu et al., 2018b). Additionally, it offers fewer public health risks when compared with the traditional nanofillers, such as nanoclays, nanoaluminum oxide particles, silica, mica, and carbon blacks (Ng et al., 2017). At the laboratory level, the techniques for micro and nanocellulose production are firmly settled, despite being constantly subjected to new optimization processes. The path to obtaining these particles from biomass traditionally could be performed in two leading steps. The first one is the pre-treatment of the raw material to secure the purest cellulosic fibers, removing the bulk of hemicellulose, lignin, and other minor components. In the second step, the fibers are converted into one of two main specimens of micro and nanocellulosic materials (Dufresne, 2013; Klemm et al., 2018).

The extraction yield is directly correlated with the cellulose source. Cotton appears in the top as the most rational choice since it is practically pure cellulose with $>$ 90 % composition (Thomas et al., 2018). However, embracing the aim of sustainable development, environmental protection, and noncompetition with industries where cotton is highly required, the pursuit of alternative cellulose resources should continue. As a possible solution, lignocellulosic waste has attracted much attention in the extraction and utilization of MCC/CNC (Wang et al., 2017).

Therefore, the main objective of this experimental work was the development of biocomposites, made of chitosan reinforced with micro and nanocelluloses extracted from the stems of three different lignocellulosic biomasses, *Arundo donax* L. (giant reed), *Hibiscus cannabinus* L. (kenaf), and *Miscanthus x giganteus* Greef et Deu. (miscanthus), for application in packaging, e.g. food packaging. Since an effective separation of micro and nanocelluloses is difficult to observe, as the forces that aggregate the nanoparticles are very strong, and with the aim of making the most of the particles obtained via hydrolysis, the extra step needed to separate micro from nanoparticles was not executed, and the mixture of MCC/CNC was used. The biomass from these crops were chosen because they are commercially available, through its use on the production of energy or materials, and also because these crops are considered low indirect land-use change (ILUC) crops, acting also as soil phytoremediation agents, offering a range of ecological services (Fernando et al., 2004, 2016; Cumbane et al., 2020).

There are some works that have applied nanocellulose isolated from giant reed (Martínez-Sanz et al., 2018a, 2018b), kenaf (Karimi et al., 2014; Zarina and Ahmad, 2015) and miscanthus (El Achaby et al., 2017; Klochko et al., 2020) in different biopolymer matrices. Moreover, only one work combined crystalline nanocellulose extracted from kenaf with chitosan, but to form a hydrogel applicable in wound healing (Bhatnagar et al., 2021). To our knowledge, scatter information is available in literature on the use of micro and nanocellulose together from these industrial crops as reinforcement agents in biobased polymers, and therefore, this work aimed to advance knowledge in this field.

2. Materials and methods

2.1. Materials and reagents

Commercial high molecular weight (31–37 kDa) chitosan (poly(D-glucosamine)) with 75 % of deacetylation, ethanol, and sodium hydroxide (NaOH) were purchased from Sigma Aldrich (Germany). Commercial Nanocellulose was kindly supplied by Nanocrystacell (Slovenia). Glacial acetic acid, glycerol, calcium nitrate ($Ca(NO_3)_2$), sodium bromide (NaBr), potassium acetate (CH_3COOK, 99 % purity), sulphuric acid 95–97 % (H_2SO_4), and hydrogen peroxide (H_2O_2) were purchased from Alfa Aesar (Germany). All chemicals were of analytical reagent grade and were used as purchased. The water was purified employing the Milli-Q system (Millipore, USA). Kenaf, miscanthus and giant reed biomass were obtained from the harvest of pilot fields of these crops established in Caparica, near Lisbon, in the Peninsula of Setúbal, Portugal. The biomass of kenaf and miscanthus were collected in November 2018. The biomass of giant reed were collected in January 2020. The collected material was dried at 40ºC in a vacuum oven, cut in small pieces and stored in darkness, in a dry place at room temperature until use.

2.2. Micro and nanocellulose isolation

The methodology implemented for MCC/CNC isolation was accomplished by incorporating and adapting procedures reported for different biomass sources (Collazo-Bigliardi et al., 2018; Ferreira et al., 2018; Xu et al., 2018b). The process counts with three main stages, alkali pre-treatment, bleaching, and acid hydrolysis.

To remove superficial impurities, the raw fibers were firstly washed with hot distilled water for one hour at 60ºC with mechanical stirring and then dried in an oven (WTB binder, Germany) at 80 ºC until constant weight. The washed dry raw fibers were cut into small pieces of about 5 mm width and random length and then submitted to a smashing process by a high-speed disintegrator (Hukoer, China) and sieved to the particle size of 60–80 mesh (150–200 μm). Conventionally, the cellulose isolation method comprehends an extra Soxhlet extraction step to remove wax, pigments, and oils. Taking into account the work of Martínez-Sanz et al. (2018a), (2018b) which referred that the Soxhlet treatment did not represent a significant difference between samples, and with the aim of achieving equal process efficiency and cost minimization, it was decided to skip this step.

Further, the alkali pre-treatment was performed by mixing 60 g of each sample powder with a 7 % (w/v) NaOH solution (mass ratio of 1:10). The system was maintained for 3 h at 70ºC under continuous mechanical stirring. After, the pre-treated fibers were filtered and washed with hot distilled water until the alkali solution was removed. This pre-treatment was repeated one more time. After the second pre-treatment, the fibers were dried in an oven at 80ºC until registered a constant weight.

In the third stage, the resulting pre-treated fibers were bleached for 4 h at 60ºC in a solution consisting of 4 % (w/v) NaOH and 24 % (v/v) H_2O_2 at a proportion of 1:1 (v/v). In this method, a fiber/solution ratio of 1:20 (w/v) was maintained. The fibers were mixed in the NaOH solution and the H_2O_2 will be added by dripping. This treatment was repeated three times. After the third bleaching, the fibers were dried in an oven at 80ºC until registered a constant weight.

The most conventional and effective technique to produce nanocrystalline cellulose is through acid hydrolysis. During the hydrolysis procedure, the amorphous zones of cellulose are preferentially digested because they are more sensitive to acidic attacks, reaching the nanoscale (Dufresne, 2013). However, after the end of the reaction, not all fibers react to the point of being converted into nanometric size. Despite being more fractionated when compared with the initials fibers, these particles are still a few micrometers long. Knowing this, it was decided to test the mixture of the biomass derived MCC/CNC as reinforcement of the chitosan films, without separating them, to avoid an additional processing step. Accordingly, bleached fibers were hydrolyzed with 64 % (w/w) H_2SO_4 solution in fiber to acid ratio of 1:20 (w/v) for 45 min. The procedure started at ambient temperature (around 25ºC) and slowly increased until 45ºC. The reaction was terminated by the addition of 1:10 (v/v) very cold distilled water. The obtained suspension was centrifuged with distilled water at 10.000 rpm at 0 °C for 15 min (repeated several times) to remove the excess H_2SO_4. The resulted precipitant was centrifuged several times until it reached a pH of 5, then neutralized with a few drops of 7 % (w/v) NaOH. Finally, it was homogenized under constant mechanical stirring for 5 min with ultraturrax (15.000 rpm) (IKA®T18, Staufen, Germany), followed by 30 min in ultrasounds (360 W) (Selecta, Spain).

Finally, the mixture of both particles was carefully dried in an oven at 50ºC until was achieved a gel, with 80–90 % of water. The gel was frozen until further essays to ensure that it is stored over time without degradation (Ditzel et al., 2017; Mohaiyiddin et al., 2018).

2.3. Biocomposites preparation

The films were prepared according to Souza et al. (2019). Film-forming dispersion (FFD) was prepared by dissolving 1.5 % (w/v) of chitosan in 1 % (v/v) of a glacial acetic acid solution under vigorous mechanical stirring for 24 h at room temperature. After, glycerol, as a plasticizer, was added at the percentage of 30 % (w/w) of chitosan in all treatments. This amount of glycerol added (corresponding to only 0.45 % w/v in the FFD) was chosen based on previous experiences with chitosan bionanocomposites (e.g. Souza et al. (2019), as it was found this amount optimal for film formation, and to obtain improved barrier and mechanical properties. Moreover, as the amount of glycerol was constant in all the composite films, differences among them will be determined by the effect of the extracted biomass-derived MCC/NCC incorporated in the chitosan (that also has glycerol). To transform the bio-based films into biocomposites, the MCC/CNC from the three different biomasses in the levels tested (1.5 %; 2 % or 2.5 % w/w chitosan) were added to FFD. Thereafter, three agitation cycles of 5 min agitation with ultraturrax (15.000 rpm) were pursued by 15 min degasification in an ultrasound bath (360 W) was performed. These three cycles were adopted to assure a suitable exfoliation and dispersion of the MCC/CNC into the polymeric chain. The finished dispersion was then cast in glass molds (18 ×25 cm) and left to dry with the aid of a circulatory hot fan for approximately 24 h. When totally dried, the biocomposites were peeled and saved protected from light in a desiccator containing saturated calcium nitrate solution at 25ºC and 50 % relative humidity, monitored with a thermohygrometer, until future evaluations.

Aiming to study the reinforcing impact of mixing micro and nanocellulose together, a Ch film without any amount of reinforcement and Ch film reinforced with commercial nanocellulose (at the same percentages) were produced for comparison.

2.4. Cellulose material characterization

2.4.1. Compositional characterization

The main constituents present in giant reed, kenaf, and miscanthus fiber was performed at two different stages, initial, and after alkaline pre-treatment/bleaching, following the Van Soest methodology (Soest, 1963).

2.4.2. Microcellulose morphology: polarized optical microscopy

The initial untreated fibers and the MCC particles obtained after the acid hydrolysis stage were observed under an Olympus BX51 polarized optical microscope (POM) (Tokyo, Japan) connected to a SCHOTT KL2500 LCD cold light source. An equipped camera (Olympus DP73) along with Olympus Stream Basic 1.9 software was used for image capture. To perform a feasible identification, the initial fibers were dispersed in water while the MCCs were identified using the final suspensions after de acid hydrolysis. Each sample was placed into individual rectangle hollow glass tubes (VitroTubes™, 50 × 4 mm^2, 0.4 mm path length). Five images of each sample were taken. The images were treated using ImageJ software (Maryland, USA) to quantify the cellulose microparticles identified in the measured region and consequently measure their average size. This software analyzes the POM images by identifying, counting the microparticles and drawing an outline on them. Through a scale introduced in the software, the width and length can be measured using the defined outlines.

2.4.3. Nanocellulose morphology: atomic force microscopy

Atomic force microscope (AFM) topography of the film surface was acquired with an Asylum Research MFP-3D Standalone system (Oxford Instruments, UK) operated in room conditions, in alternate contact mode, using commercially available silicon probes (Olympus AC160TS, f0 = 300 kHz, k = 26 N/m). Topographs were low-level plane fitted and exported to images using the Gwyddion software.

2.5. Biocomposites characterization

2.5.1. Thickness and mechanical properties

A Mitutoyo digital micrometer (Mitutoyo, Kawasaki, Japan), with a 0.001 mm precision, was used to measure the thickness of the biocomposites in ten random points of each sample. The mechanical properties were set according to ASTM D882–18 (ASTM International, 2018). Five strings of each sample (150 mm wide and 25.4 mm long) were mounted in the tensile grips with a 0.5 kN load cell (Autograph Shimadzu, Sydney, Australia), with a 50 mm initial gauge length and stretched at a cross-head speed of 50 mm/min until breakage. The tensile testing was performed and the values of Young's modulus also known as elastic modulus (EM), tensile strength (TS), and percentage of elongation at break (EAB) were calculated.

2.5.2. Morphological characterization: scanning electron microscopy

The morphological characterization was done following the work of Souza et al. (2019). Basically, to analyze the biocomposite morphology, scanning electron microscopy (SEM) micrographs of the film's cross-section. The images were acquired from a Zeiss instrument (Model DSM 962, Oberkochen, Germany) under vacuum, accelerated at 3 kV. The samples were set with a double adhesive coated carbon tape on aluminum stubs and covered with gold-palladium using a sputter coater. Cross-section images were carried out in samples previously submitted to fractions after contact with liquid nitrogen.

2.5.3. Optical properties

The optical properties of the biobased films were determined following the work of Souza et al. (2017). The color of each specimen was observed through the colorimeter CR410 (Minolta Co., Tokyo, Japan) with a 10 mm diameter window and D65 illuminant/10º observer, which exposes the CIE-L*a*b* coordinates (L* indicates black (0) to white (100); a* indicates red (+) to green (-) and b* indicates yellow (+) to blue (-)) useful to calculate the optical parameters chroma (c*) and Hue angle (hue). The measurements were taken on a white background pattern and the equations used are the following:

$$c^* = (a^{*2} + b^{*2})^{1/2} \tag{1}$$

$$hue = \arctan\left(\frac{b^*}{a^*}\right) X \frac{180}{\pi}, \quad for \quad a^* > 0 \quad and \quad b^* > 0 \tag{2}$$

$$hue = \arctan\left(\frac{b^*}{a^*}\right) X \frac{180}{\pi} + 180, \quad for \quad a^* < 0 \tag{3}$$

$$hue = \arctan\left(\frac{b^*}{a^*}\right) X \frac{180}{\pi} + 360, \quad for \quad a^* > 0 \quad and \quad b^* < 0 \tag{4}$$

Likewise, the light absorption at 600 nm per mm of film thickness, which measure the light being absorbed due to the constituents of the films, were registered by direct absorbance reading of rectangular simples at 600 nm using a UV–vis spectrophotometer (Model Spekol 1500, Analytikjena, Germany) and calculated according to the Eq. (5).

$$Abs600 \Big/ mm = \frac{absorbance \quad 600 \quad nm}{sample \quad thickness \quad (mm)} \tag{5}$$

Ultimately, the light transmittance was acquired from spectrum scans of each specimen (wavelengths between 190 and 900 nm) employing a UV–vis spectrophotometer. Air was used as a reference and the outcome expressed as a percentage of transmittance.

2.5.4. Solubility and swelling degree

In the first place, film specimens were cut into a rectangle (2 × 2 cm) and weighted (precision 0.0001 g) in an analytical balance (Mettler Toledo AB204, Switzerland), obtaining the initial weight (M1); then the samples were placed to dry at 70 ºC for 24 h in a conventional oven, and were weighted to get the initial dry mass (M2). Later, to enable the swelling process, the films were placed in Petri dishes containing 30 mL of Milli-Q water and stored for 24 h at room temperature (25 ± 2 ºC). After this contact period, the specimens were superficially dried with filter paper and weighted (M3) again. Finally, the reminiscent of each film was dried in oven at 70 ºC for 24 h to determine the final dry mass (M4). Two measurements from each film sample were taken, and the parameters were calculated according to Eqs. (6) and (7) (Souza et al., 2021).

$$\%Solubility \quad \left(\frac{g}{100 \quad g} \quad of \quad film\right) = \quad \frac{(M2 - M4)}{M2} \quad X \quad 100 \tag{6}$$

$$\%Swelling \quad degree \quad \left(\frac{g}{100 \quad g} \quad of \quad film\right) = \quad \frac{(M3 - M2)}{M2} \quad X \quad 100 \tag{7}$$

2.5.5. Water contact angle

The sample hydrophilic character was assessed from water drop contact angles on the film's upper surfaces, using the sessile drop technique. This feature denominated water contact angle (WCA), was measured by the sessile drop method using a goniometer (KSV Instruments Ltd., CAM 100, Finland) with the software KSV CAM 100. The experiments were performed at room temperature (25 ± 2 ºC / RH ~ 52 %) over the course of 5 s after a water drop was placed on the upper surface of the film. For each film type, at least five measurements at a different position on the surface of the films were performed.

2.5.6. Water vapor permeability

Water vapor permeability (WVP) was determined using a gravimetric method at 30 ºC as described by Ferreira et al. (2016). Briefly, the films were sealed on the top of 45 mm diameter glass cells containing 8 mL of saturated NaCl solution (relative humidity (RH) = 76.9 %), then, these cells were placed inside a desiccator containing saturated potassium acetate solution (RH = 22.5 %), and equipped with a fan to promote air circulation and keep a constant driving force. The temperature and relative humidity were monitored with a thermohygrometer (Vaisala, Finland). The water permeated through the film and absorbed by the desiccant was determined from the weight loss of the permeation cell (measured every 1 h during 10 h), and WVP was calculated by the following Eq. (8).

$$WVP = \quad \frac{N_W \quad X \quad \delta}{\Delta P_{w.eff}} \tag{8}$$

Where N_W (mol/m^2.s) is the water vapour flux, δ (m) is the film thickness and $\Delta P_{w.eff}$ (Pa) is the effective driving force. Results are the average ± standard deviation of the three replicates analyzed.

2.5.7. Oxygen permeability

Oxygen permeability (OP) was measured according to Souza et al. (2021). Before testing, the films were stored in an equilibrated environment at 30ºC and relative humidity of 55 % ± 5 % (desiccator containing saturated sodium bromide solution). Briefly, the film specimen was positioned in a cell between two identical stainless steel chambers, one of the chambers (feed) was filled with 0.7 bar pure oxygen (99.999 % purity) (Praxair, Spain) and the oxygen permeability was measured by the pressure change in both chambers over time, monitored using two pressure transducers (Jumo, Model 404327, Germany). To guarantee a constant temperature, the system was kept inside a thermostatic water bath at 30ºC (Julabo, Model EH, Germany). The permeability was calculated using Eq. (9):

$$\frac{1}{\beta} ln \frac{\Delta p_0}{\Delta p} = P \frac{t}{\delta} \tag{9}$$

$$\beta = A\left(\frac{1}{Vf} + \frac{1}{Vp}\right) \quad (10)$$

Where Δp (mbar) is the pressure difference between the feed and permeate compartment, P (mol.m/m^2.s.Pa) is the gas permeability, t (s) is the time, δ (m) is the film thickness and β is the geometric parameter of the cell. This parameter is calculated using Eq. (10), where V_f and V_p are the volumes of the feed and permeate compartments, respectively, and A is the film area resulting in a value of 116.2 m^{-1}.

2.5.8. Infrared absorption spectroscopy with Fourier transform

This analysis relies on the chemical bonds present in the sample that have specific vibrational frequencies. Therefore, the frequency of absorption of radiation in the infrared is particular for each type of bond, enabling the identification of interactions between the polymeric matrix and the compounds incorporated in the nanocomposites (Barbosa, 2007). Using this technique, it is expected to identify the interactions between the functional groups presents in the polymer chains and in the nanocellulose particles.

The spectra were obtained using infrared spectrophotometer model PerkinElmer spectrum Two (Perkin Elmer, USA). Infrared absorption spectroscopy with Fourier transform (FT-IR) in ATR ("Attenuated total reflectance") with 32 sweeps and 1 cm^{-1} resolution in the 4000 cm^{-1} to 500 cm^{-1} wavelength range was used.

2.5.9. X-Ray diffractometry

The samples were analyzed in a diffractometer (PANalytical Xpert PRO MRD, United Kingdom) with copper radiation (CuKα, $\lambda = 1.5418$ Å) at 40 KV, current of 40 mA, under 2θ angle ranging from 10° to 40° with a step interval of 0.02°. The specimens were mounted on silicon wafers in order to guarantee flatness and were inserted in the diffractometer.

2.5.10. Thermal analysis

The thermal properties of the films were analyzed using differential scanning calorimetric (DSC) and gravimetric (TGA) analyses, using DSC equipment (DSC 204 F1 Phoenix®, Netzsch, Germany) and PerkinElmer STA 6000 "Simultaneous Thermal Analyzer" (Germany), respectively. The glass transition temperature (Tg) of the films was determined in DSC. Film samples of approximately 10 mg were packed in an aluminum pan, sealed, and subjected to the heating cycle (20–400 °C) at a constant rate of 20 °C·min^{-1} under a nitrogen atmosphere (flow 50 mL·min^{-1}) (Woranuch and Yoksan, 2013).

In the thermogravimetric analysis, under a nitrogen atmosphere, about 10 mg of each film was heated to 400ºC at a rate of 10 °C/min and kept in isotherm for 3 min (Higueras et al., 2013). The decomposition temperatures of the compounds were measured from the first derivative of mass loss (%) (DTGA) "versus" temperature.

2.6. Data statistical treatment

All experiments were managed using an entirely randomized design with three replications. A statistical analysis of data was fulfilled through a one-way analysis of variance using IBM SPSS Statistics version 23 (IBM, USA), and differences among mean values were processed by the Tukey test. Significance was defined at $p < 0.05$.

3. Results and discussion

3.1. Fiber characterization

The chemical composition of giant reed, kenaf, and miscanthus fibers was determined at the beginning and after the bleaching stage, with the data being summarized in Table 1. The original kenaf fiber was the one that presented the highest cellulose content, 52.7 wt%, followed by miscanthus with 41.3 wt%, and giant reed with 39.2 wt%. Analogously to the amount of cellulose, kenaf fibers had the lowest lignin content, with 12 wt%. In this case, giant reed fibers were the ones that presented a higher lignin level, 27.5%. Regarding hemicellulose, the values obtained were similar between samples, with miscanthus reaching the highest quantity, 28.7 wt%. Even within the same species, the fiber composition can vary, considering several factors, such as the climate and geographic conditions of the region where the crops are produced. However, the results presented in this work are in agreement with others presented in the literature (Bernstein and Moholkar, 2020; Lv et al., 2021; Sulaiman et al., 2020; Suranjoy et al., 2020; Tsalagkas et al., 2021; Yang et al., 2020).

Upon the alkali pre-treatment and bleaching, the cellulose content continuously grew, reaching values around 90 wt% of the total fiber. These treatments were demonstrated to be efficient in removing hemicellulose and lignin, decreasing to residual values below 5%.

3.2. Micro and nanocellulose morphology

Initially, the fibers were ground until being able to pass through a sieve with a grain size of less than 150 μm. In Fig. 1, it is observed in images A1 to C1, that even though all the fibers were passed through the same sieve, the kenaf ones are shown to have a size smaller than the other two. Images A2 to C2 are relative to the same fibers after all pre-treatments and acid hydrolysis. Using the adjacent graphs where it is exposed the microparticle's average length, it was perceived that size continues smaller for the kenaf sample, with a 4.1 μm, consequently conferring a lower aspect ratio. Comparatively, giant reed and miscanthus recorded mean microparticle sizes around 31.8 μm and 34.6 μm, respectively. Subsequently, it can be established a correlation between the fiber size before the delignification steps to their size at the end of the treatments. A former characterization of the extracted biomass-derived MCC/CNC (partially presented by Pires et al., 2022a, 2022b), revealed that most of the material has been transformed into nanosize, with small variations among giant reed, miscanthus and kenaf derived MCC/CNC. But, the intricated nanofiber network and the non-spheric format of the nanofibers, causes difficulties in determining the exact ratio of MCC and CNC of the extracted biomass-derived MCC/CNC.

Fig. 2 shows the topographic surface image of different Ch biocomposites loaded with 2.5 % MCC/CNC. For all samples, it is possible

Table 1
Fiber composition before and after the pre-treatment/bleaching.

	Untreated					After Alkali and Bleaching Treatment				
	Hemicellulose (%)	Cellulose (%)	Lignin (%)	Total Fiber (%)	Ash (%)	Hemicellulose (%)	Cellulose (%)	Lignin (%)	Total Fiber (%)	Ash (%)
Giant Reed	24.8 ± 1.0	39.2 ± 1.1	27.5 ± 0.5	91.6 ± 0.4	1.9 ± 0.3	3.6 ± 0.3	90.0 ± 1.6	1.4 ± 0.1	95.1 ± 1.4	0.8 ± 0.4
Kenaf	25.1 ± 1.0	52.7 ± 1.1	12.0 ± 1.0	89.8 ± 0.3	1.7 ± 0.8	3.7 ± 0.3	90.2 ± 1.3	0.9 ± 0.3	94.9 ± 2.8	1.7 ± 0.8
Miscanthus	28.7 ± 2.1	41.3 ± 0.4	21.3 ± 1.8	91.3 ± 0.7	2.4 ± 1.4	3.2 ± 0.8	87.2 ± 2.0	3.6 ± 0.8	93.9 ± 0.4	1.2 ± 0.2

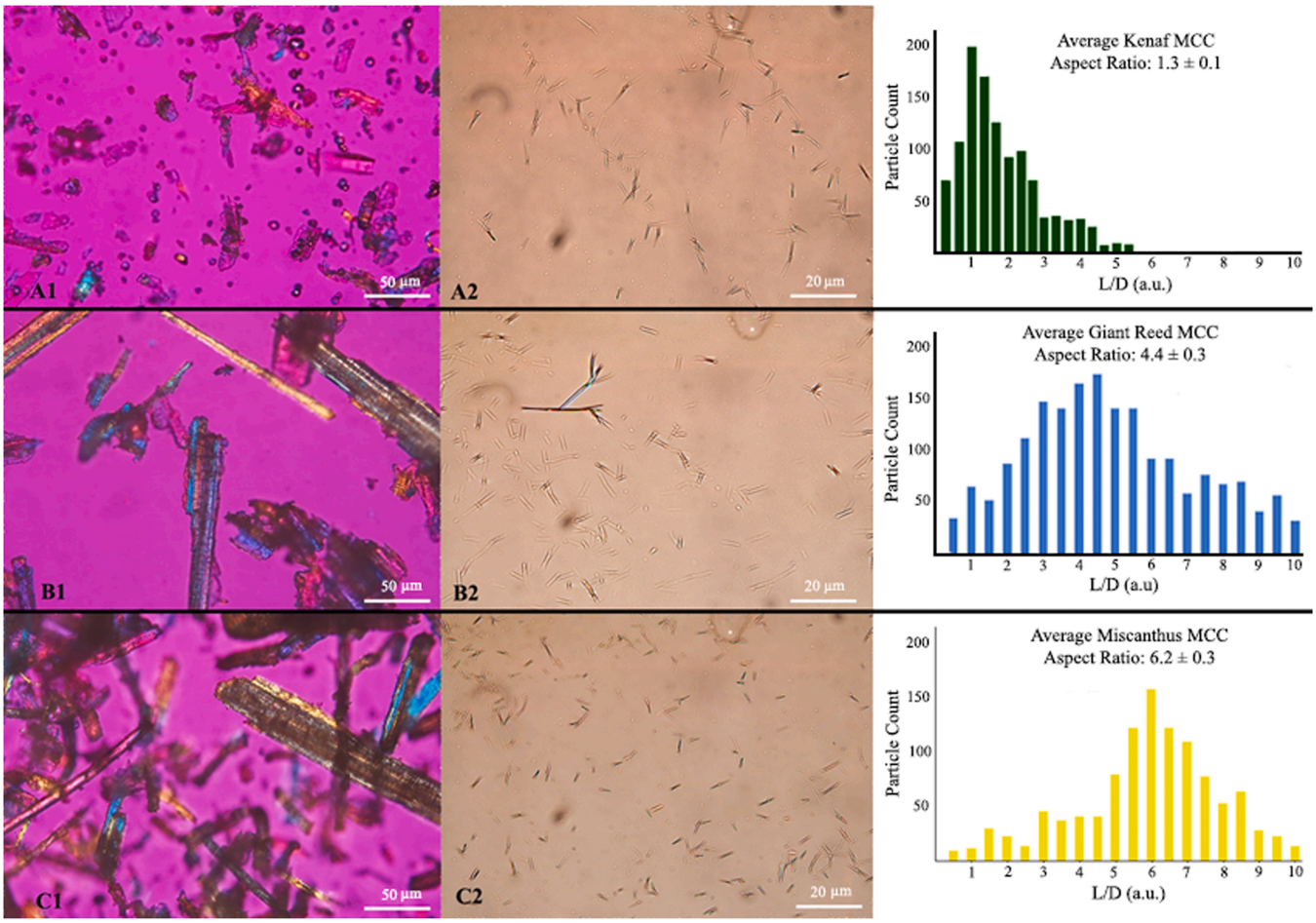

Fig. 1. Polarized optical microscopy from (A1-C1) untreated fibers; (A2-C2) fibers after the acid hydrolysis stage. Average microparticle length analysis after the acid hydrolysis stage.

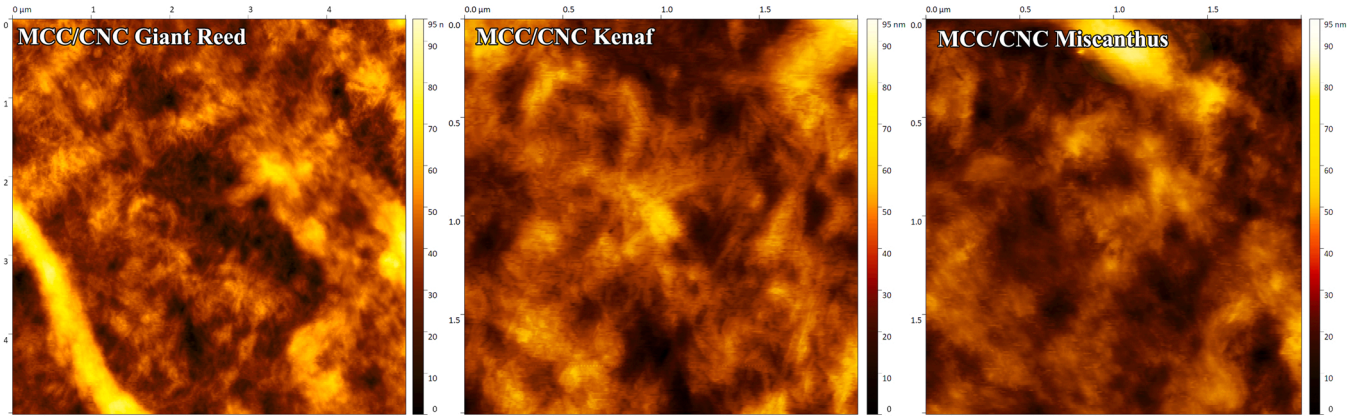

Fig. 2. Atomic force microscopy image of Ch biocomposite with 2.5% MCC/CNC from giant reed. Chitosan (Ch); Nanocrystalline Cellulose (CNC); Microcrystalline Cellulose (MCC).

to identify the nanocellulose crystals represented with a rod-shaped structure randomly dispersed throughout the polymer matrix. As CNCs occupy interstitial spaces in the polymer matrix, it is very unlikely that they will be able to identify individual nanoparticles. Along with this, it is possible to observe that the aggregation phenomenon characteristic of CNC occurred during the drying process, leading to zones of the film being more loaded than others. Hereupon, it is very difficult to access and measure the average length and diameter to calculate the aspect ratio of the nanoparticle. As it is recognized, for greater stress transfer from film matrix to reinforcing material, a minimum aspect ratio is necessary (Mujtaba et al., 2017).

3.3. *Biocomposites characterization*

3.3.1. *Mechanical properties*

Before the performance of mechanical tests, the biocomposites were characterized in terms of thickness and density (Table 2). As predicted, it was observed that samples loaded with MCC/CNC presented a slight but

Table 2
Mechanical properties obtained for different Ch/MCC/CNC biocomposites with different MCC/CNC concentrations (0, 1.5, 2, 2.5 wt%).

Specimen	Thickness (μm)	Density (g/cm^3)	Tensile Strength (MPa)	Elastic Modulus (MPa)	Elongation at Break (%)
Pristine Ch	40.3 ± 1.1^{c}	1.30 ± 0.09^{c}	34.6 ± 3.7^{cd}	1415.4 ± 94.0^{e}	27.9 ± 1.6^{a}
Ch + 1.5% CNC Commercial	56.1 ± 04^{b}	1.32 ± 0.05^{bc}	34.0 ± 0.3^{d}	1636.0 ± 76.5^{cd}	21.6 ± 0.4^{b}
Ch + 2% CNC Commercial	55.8 ± 0.6^{b}	1.31 ± 0.03^{bc}	43.8 ± 0.5^{b}	2221.8 ± 141.2^{a}	16.7 ± 2.6^{c}
Ch + 2.5% CNC Commercial	58.2 ± 0.8^{a}	1.42 ± 0.01^{ab}	37.2 ± 2.3^{c}	2035.3 ± 107.3^{ab}	10.9 ± 2.2^{de}
Ch + 1.5% MCC/CNC Giant Reed	52.9 ± 0.9^{b}	1.31 ± 0.06^{bc}	40.8 ± 4.4^{bc}	2022.0 ± 92.1^{ab}	8.9 ± 1.7^{de}
Ch + 2% MCC/CNC Giant Reed	53.6 ± 0.3^{b}	1.46 ± 0.08^{a}	42.2 ± 4.5^{b}	1983.5 ± 34.1^{b}	9.8 ± 1.2^{de}
Ch + 2.5% MCC/CNC Giant Reed	54.2 ± 0.2^{b}	1.46 ± 0.04^{a}	47.5 ± 1.5^{a}	2216.0 ± 83.9^{a}	7.0 ± 2.2^{e}
Ch + 1.5% MCC/CNC Miscanthus	54.9 ± 1.7^{b}	1.30 ± 0.03^{c}	31.2 ± 1.9^{e}	1258.3 ± 104.2^{e}	10.7 ± 2.6^{de}
Ch + 2% MCC/CNC Miscanthus	56.0 ± 0.4^{b}	1.32 ± 0.07^{bc}	33.2 ± 1.0^{d}	1541.8 ± 19.4^{d}	9.3 ± 2.0^{de}
Ch + 2.5% MCC/CNC Miscanthus	57.7 ± 1.4^{ab}	1.34 ± 0.08^{bc}	37.9 ± 0.2^{c}	1745.3 ± 68.5^{c}	6.6 ± 1.9^{e}
Ch + 1.5% MCC/CNC Kenaf	54.6 ± 0.8^{b}	1.36 ± 0.05^{bc}	36.5 ± 0.7^{c}	1964.9 ± 32.1^{b}	11.7 ± 1.5^{d}
Ch + 2% MCC/CNC Kenaf	55.3 ± 0.9^{b}	1.39 ± 0.06^{b}	39.0 ± 1.4^{c}	2053.6 ± 51.8^{ab}	9.5 ± 0.7^{de}
Ch + 2.5% MCC/CNC Kenaf	56.7 ± 1.1^{ab}	1.43 ± 0.03^{ab}	43.2 ± 1.9^{b}	2125.7 ± 43.9^{ab}	7.1 ± 1.5^{e}

Chitosan (Ch); Nanocrystalline Cellulose (CNC); Microcrystalline Cellulose (MCC). Different superscripts in the same column indicate significant differences among samples ($p < 0.05$).

significant increment ($p < 0.05$) in these features, since it was added a new solid component to the matrix. Posteriorly, each specimen was subjected to a mechanical assay to evaluate the impact that the added particles had on the biocomposite tensile strength (TS), elastic modulus (EM), and elongation at break (EAB).

The stress-strain curves revealed that the pristine Ch film had 34.6 ± 3.7 MPa for TS, 1415.4 ± 94.0 MPa for EM, and 27.9 ± 1.6% for EAB. The fillers proved to be effective as a reinforcement agent, as shown in Table 2. The film strength and stiffness were improved, while the ductility decreased. The film loaded with 2.5% giant reed MCC/CNC registered the highest TS value, 47.5 ± 1.5 MPa (more 37% than control). The highest EM observed was 2221.8 ± 141.2 MPa (more 57% than control) for the sample with 2% commercial CNC with no significant difference ($p > 0.05$) for the biocomposites reinforced with 2.5% MCC/CNC from giant reed or kenaf.

The control Ch/Commercial CNC attained a mechanical maximum to the percentage of 2%. Above that concentration, there was a decrease in the film's strength and stiffness, possibly due to the fact that the number of nanoparticles exceeded the acceptable limit for the matrix and therefore agglomerates were formed, which began to deteriorate the mechanical properties. Comparatively, Ch/MCC/CNC extracted from the lignocellulosic biomass demonstrated a mechanical upgrade proportional to the amount added, being achieved a maximum for the 2.5% load, hence, not predicting the occurrence of particle aggregation below this amount. The results reveal a similar trend as indicated in other works which verified that introducing nanocellulose concentrations up to 3% raised the film's strength and stiffness (Mao et al., 2019; Xu et al., 2018b). Interestingly, Khan et al. (2012) and Xu et al. (2018b) observed that to CNC concentrations above 5% the TS and EM decreased, which was attributed to the existence of nanocellulose aggregates that promoted fracture points in the biocomposite.

The MCC/CNC reinforcing effect on the mechanical properties can be explained through different factors. Intrinsically, these particles possess a considerable aspect ratio, opening a route to more uniform stress distribution, allowing a superior stress transfer through the matrix/reinforce interface. It was seen through the morphological analysis that kenaf's MCC has a lower aspect ratio than the others (Fig. 1), which may help to justify the greater mechanical reinforcement of giant reed MCC. On the other hand, it is strange that the same did not happen for miscanthus's MCC. Moreover, they own a huge specific surface area that grants to the filler enhanced mechanical properties even at low concentrations (Khan et al., 2012; Mujtaba et al., 2017; Talebi et al., 2021). By filling the spare space amidst the polymer chains, the suitable electrostatic interaction of polyelectrolyte complexes between the MCC/CNC anionic sulfate groups and Ch cationic amine groups generated a strong interface between them. Additionally, if it is granted a correct homogeneous dispersion, the chance to develop percolating networks with the free hydroxyl groups into the biopolymer matrix will increase. This ability could be responsible for the creation of more enduring intermolecular and intramolecular bonds (Costa et al., 2021; Pires et al., 2019a, 2019b; Salari et al., 2018).

The EAB describes the material's capacity to support shape modifications without fracture development. Contrary to the increase presented by the TS and EM, it was noticed that the introduction of MCC/CNC made the films less elastic, thus, for greater concentrations, lower will be the film's ductility. The lowest EAB percentage was achieved with a 2.5% amount without a statistical difference ($p > 0.05$) between samples, with an approximated 75% reduction when compared with the control sample. These results are in agreement with Salari et al. (2018), which justifies the EAB reduction with the presence of nanoparticles that fabricated a dense layout with increased continuities within the polysaccharide network. However, Mujtaba et al. (2017) and Talebi et al. (2021) observed opposite results. In these studies, with more significant reinforce amounts, higher values for EAB were registered. In Mao et al. (2019) study, two different phenomena occurred that can help to explain this disparity. The authors have prepared two Ch/CNC biocomposites by two different methodologies, in which one system displayed cellulose nanoparticles more dispersed than the other. For the equivalent amount, the membrane with the better particle dispersion showed superior EAB values when compared with the pristine Ch, and the membrane with lower particle dispersion acquired inferior EAB values compared with the control. Accordingly, a righteous reinforce dispersion could be an indication of better stress transfer between polymer matrix and nanofillers, thus, reaching higher values of elasticity.

To conclude, it is predictable that the increase in film's strength and stiffness is due to the good interaction among MCC/CNC anionic sulfate groups and Ch cationic amine groups, and the decrease of elasticity owns to the cellulose nanoparticles that are not very well dispersed and oriented, diminishing the stress transfer between the matrix and the filler leading to more compacted structures. It is also important to stress that the origin and the methodology used to isolate cellulose and successive hydrolysis influence the intrinsic characteristics of the MCC/CNC particles, as the crystallinity, which controls their mechanical reinforcement capacity. Further, Ch/MCC/CNC biocomposite unique formulation can elucidate the differences detected in the literature (Pires et al., 2021). Achieving a completely homogeneous dispersion represents a challenging task that needs to be optimized. Naturally, the micro/-nanoparticles tend to agglomerate due to the high specific surface area and surface energy. Therefore, when these are in powder form, as has been done in this work, unrepairable phenomena of agglomeration, reorganization, and co-crystallization take place. Ultrasound of the MCC/CNC suspensions, prior to the introduction in the biopolymeric matrix, could be at the origin of better mechanical results (Kargarzadeh et al., 2017).

3.3.2. Morphological characterization

Morphological characterization was performed by scanning electron microscopy technique to the Ch films cross-sections with MCC/CNC, in the amount of 2.5%. The SEM images presented in Fig. 3 were zoomed in on the lower part of the cross-section of each film, as this is the most homogeneous part due to the casting drying process used, and therefore the most consistent area in which the effect of adding the micro and nanoparticles is verified. Image A corresponds to Ch film with commercial CNC. It was observed a homogeneous fillers dispersion through the matrix, with a smooth and nonporous surface and without cracks, indicating that this biocomposite was dense and compact. In contrast, for the remaining biocomposites, the combination of micro and nanoparticles led to an increase in roughness and the appearance of some cracks, which could be detrimental to the biocomposite mechanical properties and stability. It should additionally be noted that the spherical particles observed in image D, referring to miscanthus, have a more considerable size when compared with those observed in image C, referring to kenaf. In image B, corresponding to the film with particles extracted from giant reed, a phenomenon of wrinkles formation was observed at the cross-section bottom of the film. The appearance of wrinkles is usually the outcome of an inhomogeneous deformation, provoked by stress and shrinking, in surface layers with distinct mechanical properties, providing different surface reliefs concerning the stress directions (Izawa et al., 2021). A hypothesis for this spontaneous phenomenon can be attributed to a gradient of concentration promoted by different deposition of the micro/nanoparticles between the top and the bottom of the film, which can occur during the drying process. This gradient leads to different mechanical properties, between the top and the bottom of the film, and the formation the micro wrinkles Although this behavior has been reported for another biomatrix (Rizzieri et al., 2006), there is not enough information to help explain this phenomenon in chitosan films. One of the few reports found in the literature that addresses this topic is the recent work of the Japanese team Izawa et al. (2021). The author's prepared chitosan films with induced surfaced wrinkles by regulating the drying stress on oriented substrates, conducting a novel controlled surface wrinkling system using a drying process.

3.3.3. Optical properties

The optical properties analysis is crucial when it is intended to use as a packaging system because these may interfere with consumer acceptance, in the means that the film can filter and alter the appearance of the product inside the packaging (Souza et al., 2019). The hue angle, as exhibited in Table 3, confirms the biocomposites visual aspect which corresponds to a slightly yellowish color. All the MCC/CNC levels added to the films were shown to be ineffective in significantly changing ($p > 0.05$) the color parameter as indicated by the hue angle outcome. Regarding the luminosity, the filler only started to affect the film lightness for the 2.5% amount.

The measurement of film's light absorption at 600 nm per mm of the film thickness, indicates that higher absorption values were analogized with lower light transmittance levels. The results exhibited in Table 3 reveal that Ch/MCC/CNC biocomposites absorbed light more than the pristine Ch film. Indeed, it is clearly identified that the opacity values rise is proportional to the content, having been achieved the maximum for the 2.5% MCC/CNC load with no significant difference ($p > 0.05$) for the 2%.

The presence of UV light could be a accelerator of oxidation processes, therefore, if the films can confer protection against this external phenomenon it could be recognized as an advantage (Salari et al., 2018). Accordingly, the ultraviolet light transmittance was evaluated for films reinforced with 2,5% MCC/CNC and then compared with the control

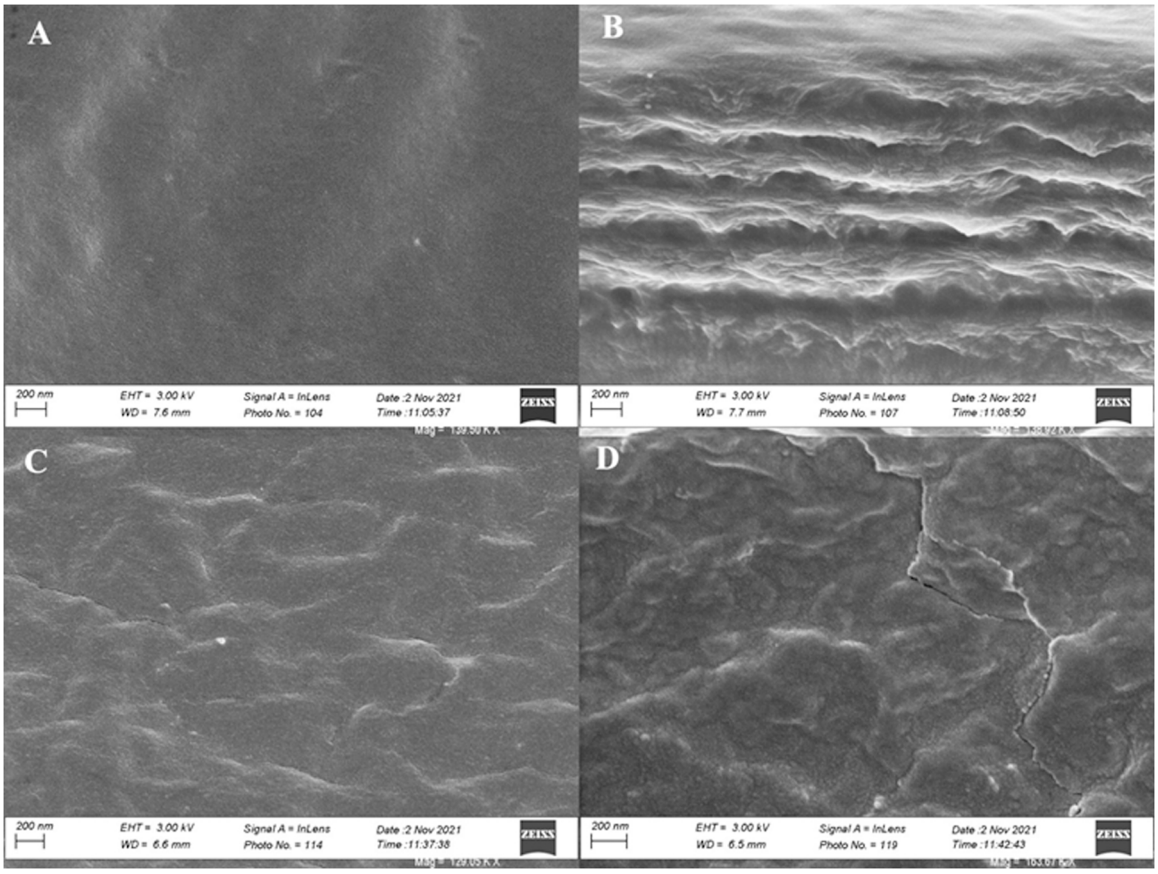

Fig. 3. Scanning electron microscopy (SEM) of cross section of (A) Ch + 2.5% CNC Commercial; (B) Ch + 2.5% MCC/CNC Arundo; (C) Ch + 2.5% MCC/CNC Kenaf; (D) Ch + 2.5% MCC/CNC Miscanthus. Chitosan (Ch); Nanocrystalline Cellulose (CNC); Microcrystalline Cellulose (MCC).

Table 3
Optical properties obtained for different Ch/MCC/CNC biocomposites with different MCC/CNC concentrations (0, 1.5, 2, 2.5 wt%).

Specimen	Luminosity (L*)	Hue Angle	Chroma	Abs_{600}/mm
Pristine Ch	92.3 ± 0.2^{a}	98.5 ± 0.1^{a}	7.5 ± 0.5^{a}	1.0 ± 0.1^{c}
Ch + 1.5% CNC Commercial	91.2 ± 0.3^{b}	98.8 ± 0.4^{a}	8.1 ± 0.1^{a}	1.3 ± 0.1^{bc}
Ch + 2% CNC Commercial	91.6 ± 0.1^{b}	97.5 ± 0.3^{a}	8.0 ± 0.1^{a}	1.7 ± 0.4^{ab}
Ch + 2.5% CNC Commercial	91.5 ± 0.3^{b}	97.9 ± 0.3^{a}	7.8 ± 0.5^{a}	1.5 ± 0.2^{ab}
Ch + 1.5% MCC/CNC Giant Reed	92.0 ± 0.1^{ab}	98.5 ± 0.7^{a}	7.6 ± 0.1^{a}	1.2 ± 0.1^{bc}
Ch + 2% MCC/CNC Giant Reed	91.9 ± 0.5^{ab}	97.6 ± 0.1^{a}	7.9 ± 0.1^{a}	1.5 ± 0.3^{ab}
Ch + 2.5% MCC/CNC Giant Reed	91.4 ± 0.1^{b}	98.2 ± 0.2^{a}	8.2 ± 0.3^{a}	1.8 ± 0.3^{a}
Ch + 1.5% MCC/CNC Miscanthus	92.1 ± 0.1^{ab}	98.6 ± 0.2^{a}	7.4 ± 0.2^{a}	1.0 ± 0.0^{c}
Ch + 2% MCC/CNC Miscanthus	92.2 ± 0.0^{a}	98.2 ± 0.1^{a}	7.4 ± 0.2^{a}	1.1 ± 0.2^{bc}
Ch + 2.5% MCC/CNC Miscanthus	91.4 ± 0.0^{b}	98.1 ± 0.2^{a}	8.2 ± 0.2^{a}	1.4 ± 0.0^{ab}
Ch + 1.5% MCC/CNC Kenaf	92.1 ± 0.2^{a}	98.4 ± 0.1^{a}	7.7 ± 0.4^{a}	1.3 ± 0.1^{bc}
Ch + 2% MCC/CNC Kenaf	92.0 ± 0.1^{ab}	98.0 ± 0.2^{a}	7.6 ± 0.1^{a}	1.6 ± 0.1^{ab}
Ch + 2.5% MCC/CNC Kenaf	91.7 ± 0.3^{b}	97.7 ± 0.3^{a}	8.0 ± 0.2^{a}	1.8 ± 0.4^{a}

Chitosan (Ch); Nanocrystalline Cellulose (CNC); Microcrystalline Cellulose (MCC). Absorbance at 600 nm divided by film thickness (mm) (Abs600/mm). Different superscripts in the same column indicate significant differences among samples ($p < 0.05$).

samples (with wavelengths between 200 and 400 nm) as can be seen in Fig. 4. For short-wave UV (till 220 nm) more than 90% of the light is absorbed. From this point on, it was possible to observe the micro/-nanocellulose effect on the film transmittance. For medium-wave UV (near 300 nm) the control film blocked near 60% of the light, 70–80% for biocomposites, and almost 90% for Ch/Commercial CNC. At least, for long-wave UV (400 nm), usually denominated as black light, almost 20–25% of light is absorbed for control and Ch/kenaf MCC/CNC, increasing a little to Ch/MCC/CNC from giant reed and miscanthus, and increasing substantially to 60% with Ch/Commercial CNC.

In terms of acceptance, the incorporation of reinforcing agents has changed negatively the optical properties of Ch films, once made the material more opaque. However, the extra UV protection and the environmentally friendly approach of such material may balance this negative aspect.

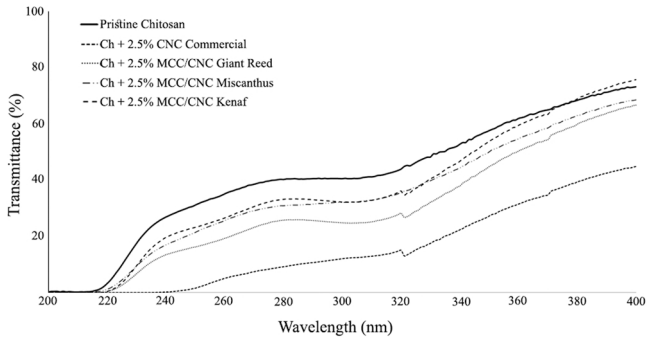

Fig. 4. Ultraviolet light transmittance (%) obtained for pristine Ch and different biocomposites with 2.5% MCC/CNC concentration. Chitosan (Ch); Nanocrystalline Cellulose (CNC); Microcrystalline Cellulose (MCC).

3.3.4. Wettability properties: Swelling, solubility, and contact angle

The wettability properties knowledge is indispensable to perceive the film behavior when in contact with aqueous food matrices. It also gives the possibility to understand the resistance to degradation under those conditions if the material is discarded in a marine environment (Souza et al., 2018). Table 4 illustrates the action of the different reinforcing agents on the film's water uptake.

Introducing fillers to the polymeric matrix had a direct effect on the sample's wettability properties, decreasing the swelling capacity and solubility, and increasing the contact angle, thus transforming the biocomposites more hydrophobic. The laboratory test for the evaluation of swelling and solubility index was designed to take place for 24 h, as, resorting to previous work, it was observed that at the end of this time, an equilibrium in the saturation levels was reached (Corsello et al., 2017; Xu et al., 2018a). Regarding these two properties, similar behaviors were observed. When the MCC/CNC percentage is 1.5%, no marked reductions were noted, and in some cases, there was even a slight increase. From 2% onwards, the decrease presented was more consequential, and with amounts near 2.5%, it can be guaranteed that water uptake is statistically different ($p < 0.05$) from those obtained by the control film. The most considerable reduction observed was attributed to film with 2.5% commercial CNC, minus 26% and 24%, for swelling and solubility respectively. Comparatively, the lignocellulosic MCC/CNC did not exhibit as expressive reductions as the commercial CNC, however, these also proved to be statistically different ($p < 0.05$) from the pristine Ch. The biocomposite swelling ability is strictly dependent on the film matrix and the characteristics of the filler, like crystallinity. Analyzing the obtained results was possible to prove that a good hydrogen bonding and electrostatic association occurred between the cellulose micro/nanoparticles and chitosan molecules, reducing the number of -OH, thereby creating a less porous network with fewer paths where water molecules can infiltrate (Mao et al., 2019; Yadav et al., 2020). These results are in line with those presented by Talebi et al. (2021), who also stated that the free amino groups, responsible for the chitosan hydrophilic nature, may have decreased with the introduction

Table 4
Wettability properties obtained for different Ch/MCC/CNC biocomposites with different MCC/CNC concentrations (0, 1.5, 2, 2.5 wt%).

Specimen	Swelling (%)	Solubility (%)	Contact Angle (Degrees)
Pristine Ch	174.9 ± 1.5^{b}	23.0 ± 1.2^{bc}	78.4 ± 2.1^{f}
Ch + 1.5% CNC Commercial	203.0 ± 17.5^{a}	21.2 ± 0.8^{cd}	84.3 ± 2.6^{cde}
Ch + 2% CNC Commercial	154.1 ± 5.9^{cd}	21.0 ± 1.2^{cd}	87.6 ± 0.8^{bc}
Ch + 2.5% CNC Commercial	130.1 ± 3.1^{e}	17.6 ± 0.7^{e}	89.9 ± 1.3^{ab}
Ch + 1.5% MCC/CNC Giant Reed	169.1 ± 15.9^{bc}	22.4 ± 1.3^{bc}	86.4 ± 3.1^{bcd}
Ch + 2% MCC/CNC Giant Reed	158.5 ± 9.5^{cd}	21.8 ± 2.3^{bc}	88.5 ± 1.1^{bc}
Ch + 2.5% MCC/CNC Giant Reed	157.8 ± 1.9^{c}	21.5 ± 0.6^{cd}	92.3 ± 1.6^{a}
Ch + 1.5% MCC/CNC Miscanthus	160.6 ± 11.1^{bc}	25.8 ± 0.5^{a}	82.1 ± 2.5^{def}
Ch + 2% MCC/CNC Miscanthus	149.7 ± 2.0^{cd}	20.4 ± 0.1^{d}	85.8 ± 2.7^{cde}
Ch + 2.5% MCC/CNC Miscanthus	145.0 ± 2.1^{d}	18.5 ± 1.0^{de}	89.3 ± 1.4^{abc}
Ch + 1.5% MCC/CNC Kenaf	171.6 ± 2.4^{b}	23.2 ± 0.3^{b}	83.7 ± 1.1^{de}
Ch + 2% MCC/CNC Kenaf	168.7 ± 7.9^{bc}	21.6 ± 0.9^{cd}	87.2 ± 0.9^{c}
Ch + 2.5% MCC/CNC Kenaf	159.3 ± 4.5^{c}	20.4 ± 0.4^{d}	90.3 ± 3.4^{abc}

Chitosan (Ch); Nanocrystalline Cellulose (CNC); Microcrystalline Cellulose (MCC). Different superscripts in the same column indicate significant differences among samples ($p < 0.05$).

of nanocellulose.

The contact angle evaluates the relative amounts of adhesive (liquid-to-solid) and cohesive (liquid-to-liquid) forces operating on a liquid and is classified over the scale $0° \leq \theta \leq 180°$. The WCA measurements obtained for pristine Ch and different biocomposites with 2.5% MCC/CNC can be seen in Fig. 5. When a drop of water falls over the biocomposite, it will propagate on the surface based on the intermolecular interactions between the film and the water (Souza et al., 2019). As illustrated in Table 4, the water contact angle of the pure Ch film was 78.4 ± 2.1°. For the majority of samples, it was visible that the minimum MCC/CNC concentration is enough to register a significant increase ($p < 0.05$) in the film's hydrophobicity. This behavior increased proportionally as the amount of micro/nanoparticles rises, being achieved a maximum for the 2.5% amount. The sample with 2.5% giant reed MCC/CNC recorded the most considerable increase ($p < 0.05$) compared with the control, about 18%, thus being considered the most hydrophobic specimen. It should also be remarkably noted that the micro/nanocellulose obtained from lignocellulosic biomass presented similar or better contact angle results compared with those of commercial nanocellulose, thus demonstrating its full potential. It is then possible to conclude that the biocomposites become more hydrophobic, due to the blocking of functional groups that would interact with the water, which is correlated with a decrease in swelling and solubility parameters.

3.3.5. *Barrier properties: Water vapor and oxygen permeability*

The capacity to prevent moisture and oxygen transfer between the inside of the packaging and the surrounding atmosphere is one of the most desirable features attributed to biodegradable films, thus, WVP and OP should remain as low as feasible. To improve that ability, the biopolymer barrier properties can be remarkably changed by the inclusion of organic or inorganic nanoparticles with a high aspect ratio that modifies the diffusion pathway of gas molecules (Pires et al., 2021). Before the presentation and discussion of the obtained results, it is necessary to clarify that the film barrier properties depend on a vast variety of factors intrinsic to its composition, like the biopolymer chemical structure, polarity, degree of crystallinity, density, and molecular weight, as well as the presence of other plasticizers or cross-linkers. These factors will determine the film affinity for the different gas molecules (Zhang et al., 2021). As the biocomposites formulation was the same except for MCC/CNC origin and quantity, it was attributed that the differences obtained should fall only on the filler reinforcing influence.

The results for water vapor and oxygen permeability follow a similar tendency introduced in the previous sub-chapter for swelling and solubility indexes and are expressed in Table 5. The two investigated variables demonstrated that the film's permeability follow a descendent trend when MCC/CNC was incorporated, and this decrease was more accentuated as the reinforcemente amount increased. This tendency is in accordance with related works found in the literature (Azeredo et al., 2010; Corsello et al., 2017; Salari et al., 2018; Yadav et al., 2020; Zhang et al., 2021).

Table 5
Water Vapor Permeability (WVP) and Oxygen Permeability (OP) coefficients obtained for different Ch/MCC/CNC biocomposites with different MCC/CNC concentrations (0, 1.5, 2, 2.5 wt%).

Specimen	WVP (10^{-11} mol/m·s·Pa)	OP (10^{-16} mol/m·s·Pa)
Pristine Ch	1.49 ± 0.29^{b}	1.36 ± 0.10^{a}
Ch + 1.5% CNC Commercial	1.92 ± 0.10^{a}	1.21 ± 0.12^{ab}
Ch + 2% CNC Commercial	1.65 ± 0.06^{ab}	0.72 ± 0.01^{d}
Ch + 2.5% CNC Commercial	1.33 ± 0.18^{bc}	0.84 ± 0.05^{cd}
Ch + 1.5% MCC/CNC Giant Reed	1.56 ± 0.07^{ab}	1.02 ± 0.08^{bc}
Ch + 2% MCC/CNC Giant Reed	1.35 ± 0.08^{bc}	0.71 ± 0.20^{cde}
Ch + 2.5% MCC/CNC Giant Reed	0.90 ± 0.05^{d}	0.63 ± 0.13^{de}
Ch + 1.5% MCC/CNC Miscanthus	1.66 ± 0.11^{ab}	1.06 ± 0.01^{b}
Ch + 2% MCC/CNC Miscanthus	1.48 ± 0.08^{b}	1.02 ± 0.01^{c}
Ch + 2.5% MCC/CNC Miscanthus	1.05 ± 0.07^{cd}	0.58 ± 0.01^{e}
Ch + 1.5% MCC/CNC Kenaf	1.63 ± 0.05^{ab}	1.10 ± 0.01^{b}
Ch + 2% MCC/CNC Kenaf	1.42 ± 0.06^{b}	0.98 ± 0.05^{c}
Ch + 2.5% MCC/CNC Kenaf	1.09 ± 0.13^{cd}	0.74 ± 0.10^{cd}

Chitosan (Ch); Nanocrystalline Cellulose (CNC); Microcrystalline Cellulose (MCC). Water Vapor Permeability (WVP); Oxygen Permeability (OP). Different superscripts in the same column indicate significant differences among samples ($p < 0.05$). The units of WVP and OP may be converted to cm3·μm/(m2 bar day) by multiplying per 2 × 1020

The commercial nanocellulose revealed no significant differences ($p > 0.05$) between 2% and 2.5% amounts in both parameters, achieving a maximum reduction of 11% and 38%, for WVP and OP respectively. In the case of MCC/CNC from lignocellulosic biomasses, the most considerable permeability values decrease were attained for the 2.5% level. Giant reed held a reduction of 40% and 54%, while kenaf got a decrease of 27% and 46%, and miscanthus drew a lowering of 30% and 57%, toward WVP and OP sequentially. The explanation that supports our data could reside in the addition of fillers with a high aspect ratio that increases the film's crystallinity (acting as crystalline fillers that increase the distance for the molecules of water to pass through, i.e., a more tortuous path) (Pires et al., 2021). Once again, like in the mechanical behavior, the highest aspect ratio attributed to the MCC from giant reed could explain the lowest permeability rates. Furthermore, well scattered and arranged cellulosic MCC/CNC inside the Ch matrix, could enhance the interactions between the polymeric chains, which will decrease the free space and slow the molecular chain mobility.

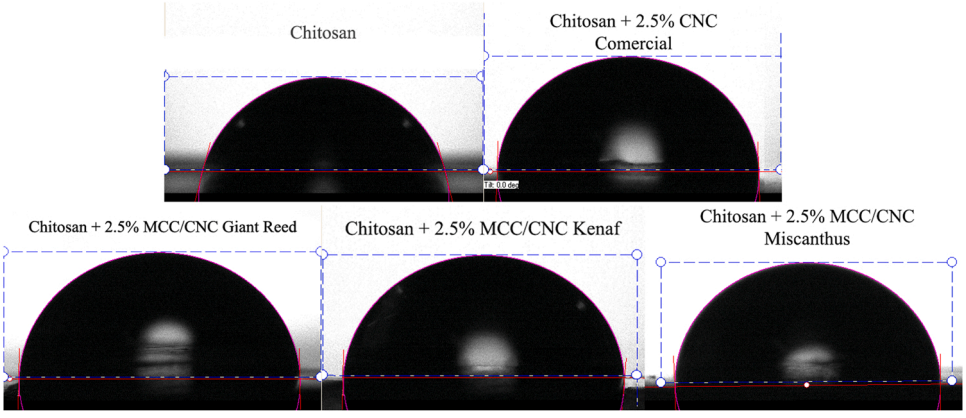

Fig. 5. Water contact angle measurements obtained for pristine Ch and different biocomposites with 2.5% MCC/CNC concentration. Chitosan (Ch); Nanocrystalline Cellulose (CNC); Microcrystalline Cellulose (MCC).

Then, the gas particles were obliged to discover new, long and harder trajectories to surround these particles, difficulting the gas diffusion through the film (García et al., 2020).

When compared with other similar studies, the reductions presented by the biocomposites appear to be rather promising, as the MCC/CNC amount introduced into Ch films was quite small. Similarly, Corsello et al. (2017) created Ch/CNC biocomposites but employed higher nanoparticles levels (1%, 3%, 5%, and 10% w/w Ch). Comparatively to the control film, a 38% reduction was the best rate that the authors achieved, correspondent to the amount of 5% CNC added. When the nanocellulose percentage increased to 10%, the WVP decreased to 25%. The presence of CNC, which added more tortuosities paths inside the biopolymeric matrix was the explanation utilized to describe the lower water vapor diffusion processes. This trend happened until a critical nanoparticle content, after which a constant or a modest increase of permeability was detected, which was also verified in the work of Costa et al. (2021) for CNC concentrations over 25%. Excessive nanofiller content could disrupt some particular points of the biopolymeric network generating the formation of gaps in which the water vapor molecules will pass through.

There is not certain that a decrease in the WVP will always happen with nanocellulose addition, as demonstrated by the work carried out by Mujtaba et al. (2017). The authors added different CNC concentrations, extracted from flax fibers, on Ch films, verifying that for the 10% CNC amount the WVP value increased by 38.7% relative to the control. The reason for this growth can own to several factors, such as the hydrophilicity of the CNC that extended the film hydrophilicity or the fact that the CNC links to places that were formerly used by Ch to bind to water molecules. According to the Mujtaba's work, the most substantial factor affecting the WVP may be the nanocellulose crystallinity, enhancing the adsorption percentage in a negative or positive way. When CNC crystallinity is small, they are not enough crystalline zones to capture water molecules, increasing the diffusion through the amorphous parts, in the contrary, for higher crystalline rates, the permeability is restricted since the crystalline parts are able to trap the water molecules (Mujtaba et al., 2017).

Studies considering an OP evaluation are still scarce in the literature, some of them do it simultaneously with WVP, as the works of Zhang et al. (2021) and Costa et al. (2021). In the first one, the authors proposed a novel Ch film reinforced with curcumin grafted TEMPO-oxidized cellulose nanofibers (CGTOCNF) at 10%, 17%, 25%, and 33%. In the second one, the authors evaluated the potential of Ch/CNC (5, 10, 25, and 50 wt%) films to be applied as active pads for meat packages. Although both indicated works applied CNC percentages in similar ranges, they obtained contradictory results. For Zhang et al. (2021) the biocomposites OP increased with the incorporation of the nanoparticle complex. Costa et al. (2021) work, in concordance with our results, showed a reduction of OP values with the CNC incorporation, confirming the nanocellulose effectiveness to decrease the film affinity for the oxygen molecules.

It can then be taken from the WVP and OP analysis that the nanocellulose characteristics, mainly its crystallinity rate, and the percentual amount included in the film, are essential to ascertain an effective reinforcement of the biocomposites final barrier properties.

3.3.6. *Thermal analysis: TGA and DSC*

In order to discover the effect of cellulose nanocrystals on the thermal properties of chitosan films, TGA curves, and DSC thermograms were fulfilled (Figs. 6 and 7), since it is a determinative evaluation to explore the thermal decomposition of polymeric materials. For this trial, only the films with the 2.5% MCC/CNC added were analyzed and compared, since this percentage proved to be most effective in optimizing the mechanical and barrier properties.

Pointing out to the final of each graph, at 400ºC, it was stated that the sample absolute mass loss was around 60%, except for the sample with 2.5% MCC/CNC miscanthus which reached 65%. The chitosan film presented a mass loss of 74.6%, being possible to demonstrate that the introduction of nanoreinforcements had a positive effect. It can be stated through Fig. 6 that the biocomposites mass loss occurred mainly in three steps. The first mass loss step appears around 50–135 °C which cause can be attributed to the evaporation of volatile molecules, like the physically adsorbed and strongly hydrogen-bonded water, and residual

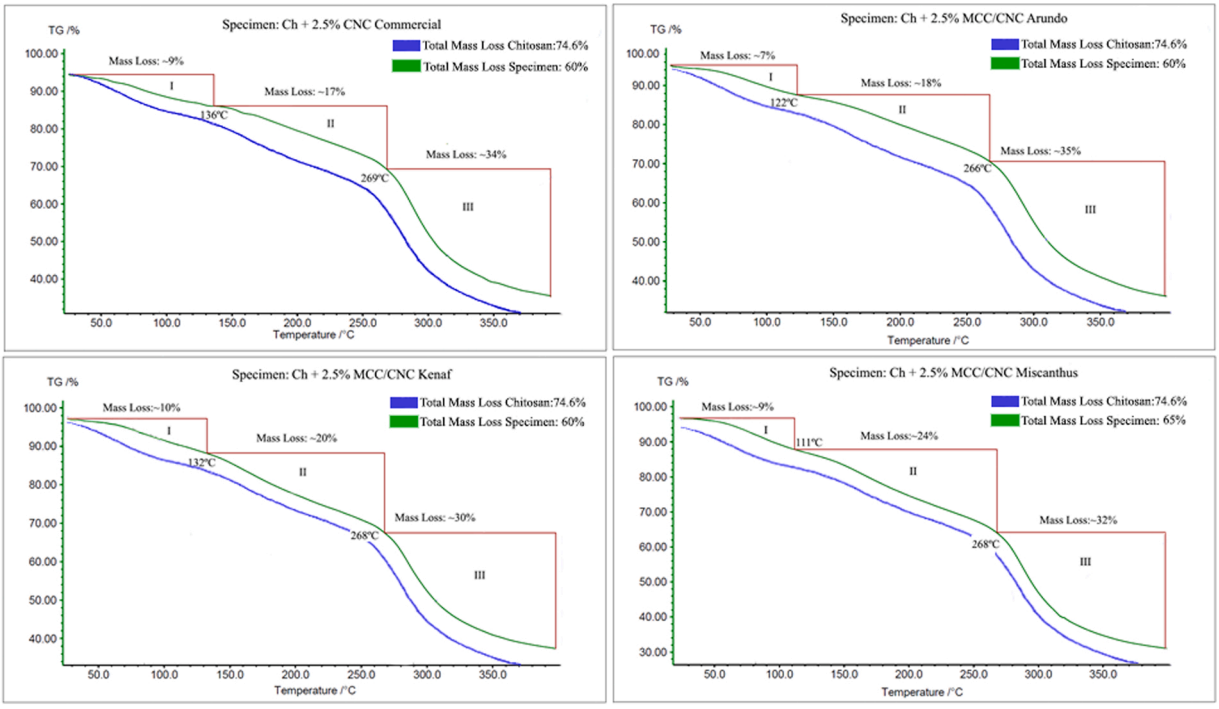

Fig. 6. TGA curves obtained for Ch film and different biocomposites with 2.5% MCC/CNC concentration. Chitosan (Ch); Nanocrystalline Cellulose (CNC); Microcrystalline Cellulose (MCC).

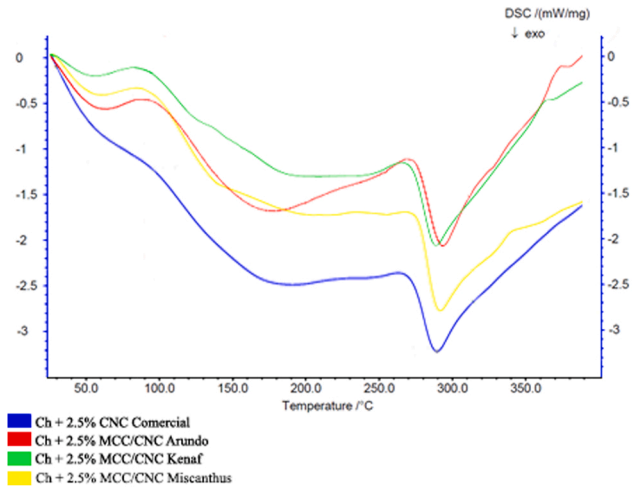

Fig. 7. DSC thermograms obtained for different biocomposites with 2.5% MCC/CNC concentration. Chitosan (Ch); Nanocrystalline Cellulose (CNC); Microcrystalline Cellulose (MCC).

acetic acid (Costa et al., 2021). The respectively endothermic broadband is positioned in a region between 81 and 91 °C. A second minor endotherm (in the range of 130–145 °C) appears in the film with MCC/CNC 2.5% from kenaf, probably due to water molecules retained by the plasticizer glycerol as it is hydrophilic in nature (Akyuz et al., 2018). The second step of noteworthy mass loss fluctuated between 130 ºC to 270 °C and may be associated with glycerol degradation and chitosan chain depolymerization through de decay of amine groups and cleavage of glycosidic linkages via dehydration and deamination. The exothermic peak relative to the decomposition temperature is perceived to be around 265–270 °C. The biopolymer degradation due to thermal split of Ch backbone, with -CH_2OH degradation, started at 290 ºC, where is verified the third mass loss, and was permanent to 400 ºC (Celebi and Kurt, 2015; Costa et al., 2021). A late slight endothermic peak, around 340–370 ºC, appeared in the biocomposites with MCC/CNC from lignocellulosic biomasses, which can be related with the particle decomposition probably due to pyrolysis as reported by some literature sources (Costa et al., 2021; Elias et al., 2017; Ismail et al., 2019). This peak is not very pronounced as the amount of MCC/CNC introduced into the film was not very high either.

Comparing the three major degradation temperatures (T10, T50, and Tmax), some differences can be observed, as exposed in Table 6. The thermal degradation patterns of the Ch/CNC Commercial and Ch/MCC/CNC from giant reed can be considered almost identical, but these two samples showed a shift to a higher degradation temperature than Ch/MCC/CNC from kenaf and Ch/MCC/CNC from miscanthus. These results demonstrated the same trend already shown by the mechanical and barrier results, in which the mixture of micro and nanocellulose from giant reed fibers possess more similarities with the commercial nanocellulose and, consequently, better results than the ones produced through kenaf or miscanthus fibers.

Glass transition temperature (T_g) and melting point (T_m) are two

Table 6
Major thermal degradation temperature of biocomposites.

Specimen	T10 (ºC)	T50 (ºC)	Tmax (ºC)
Ch + 2.5% CNC Commercial	155	334	289
Ch + 2.5% MCC/CNC Giant Reed	161	337	291
Ch + 2.5% MCC/CNC Kenaf	142	313	290
Ch + 2.5% MCC/CNC Miscanthus	122	301	290

Chitosan (Ch); Nanocrystalline Cellulose (CNC); Microcrystalline Cellulose (MCC); T10 (°C) and T50 (°C) - temperatures at 10% and 50% mass loss, respectively; Tmax (°C) - temperature at maximum mass loss rate

significant parameters used for plastic identification. The T_g value represents the temperature at occurs a change from hard to soft in amorphous polymers. The concentration of crystalline regions in amorphous (semicrystalline) polymers affects the polymer rigidity, thereby when the nanoparticles are introduced into the film it is intended to increase the crystallinity and consequently upgrade the thermal properties (Pacáková and Virt, 2005). T_m represents the temperature at which an ordered crystalline solid becomes a disordered melt and is also a barometer of atomic bonding strength establishing a relationship with the mechanical properties. The general tendency is that a higher melting temperature supposes a higher modulus and vice versa (Salamon, 2014). In our study, the T_g and T_m range were similar for all specimens, is estimated to be between 50 and 100ºC and 250–270 °C, respectively.

3.3.7. Chemical analysis: FT-IR

The chemical analysis to evaluate the structural relation established between chitosan and nanocellulose was performed with FT-IR in ATR mode. This technique is widely used to identify the chemical composition of materials as well as the intermolecular bonds. Among the range of applications of this analytical method, the ability to study the interactions between the different components present in composite materials stands out. Fig. 8 displays the different spectra obtained for the Ch pristine film and for the samples reinforced with 2.5% MCC/CNC.

The biocomposites spectra showed to be remarkably similar to the one presented by the Ch control film, with only minor modifications. Since the chemical composition of cellulose and chitosan is practically identical and the MCC/CNC amount introduced was small, the obtained result was expected. Moreover, it could be an indicator that the particles attached well with the polymer matrix attributed to strong interactions via hydrogen bonds between the functional groups of the composite components. The FTIR spectra showed that there were two leading absorptions regions in spectra, a low-wavelength section from 600 to 1700 cm^{-1} and a high-wavelength zone from 2800 to 3500 cm^{-1}. The chitosan characteristic absorption bands were identified in all spectra: at 3355 cm^{-1} (O-H stretching vibration); 3275 cm^{-1} (-NH asymmetric stretching); 2921–2885 cm^{-1} (C-H of the methyl group -NHCOCH3 symmetric and asymmetric vibrations); 1631 cm^{-1} (C═O stretching (Amide I)); 1547 cm^{-1} (N-H bending (Amide II)); 1377–1407 cm^{-1} (-CH_2 bending); 1319 cm^{-1} (skeletal vibration involving the stretching of the C-N bond (Amide III)). The last bands correspond to saccharide structure: 1251 cm^{-1} (C-N stretching), 1150 cm^{-1} (asymmetric stretching of the C–O–C bridges), and 926–1033 cm^{-1} (C-O stretching at C-3 position) (Costa et al., 2021; Khan et al., 2012; Xu et al., 2018b). In the biocomposites spectrum, the differences for the control were practically non-existent, however, it appears that the peak at 1377 cm^{-1} disappears, and two very subtle peaks appeared at the wavelengths of 1220 cm^{-1} and 1360 cm^{-1}. Following the observations of Morais et al. (2013) these peaks could be related to the presence of sulfonates present in the micro/nanocellulose, generated during the hydrolysis step. Messa and Faez (2020) also identified the appearance of a new band at 1202 cm^{-1} and related that peak with the S═O stretching vibrations, due to the sulfate groups on nanocellulose as a consequence of sulfuric acid hydrolysis.

3.3.8. Crystallinity analysis: XRD

The application of the X-ray diffraction technique (XRD) aims to examine the level of micro/nanoparticles exfoliation between the polymer chains of chitosan. The improvement of the mechanical, barrier, and thermal properties are narrowly connected to the degree of exfoliation, such a fundamental determination (Yadav et al., 2020).

The pristine Ch sample and the films reinforced with 2.5% MCC/CNC diffractograms are presented in Fig. 9. The Ch film without MCC/CNC incorporation presented two characteristic diffraction peaks at 2Θ = 11.4°, 18.0°, and a shallow peak between 20º-22.5º. The first peak corresponds to a crystalline structure and the last one to the amorphous structure associated with the semi-crystalline nature of chitosan.

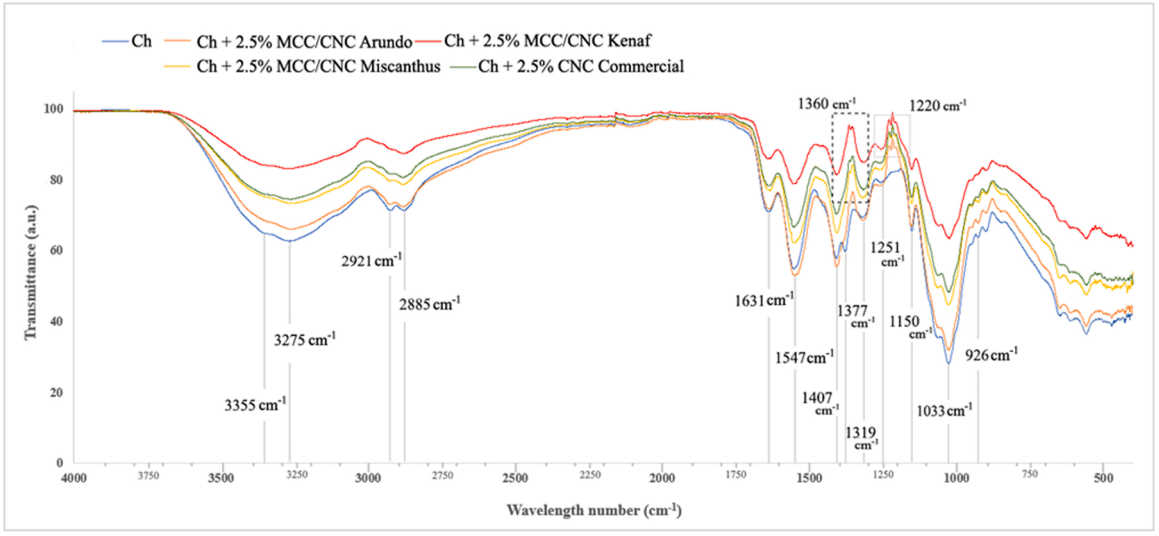

Fig. 8. FT-IR spectra of Ch pristine film and for different biocomposites with 2.5% MCC/CNC concentration. Chitosan (Ch); Nanocrystalline Cellulose (CNC); Microcrystalline Cellulose (MCC).

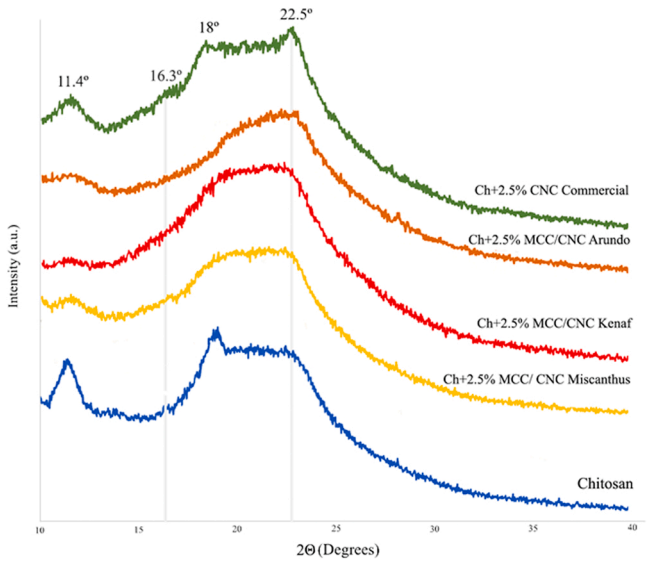

Fig. 9. XRD patterns of Ch pristine film and for different biocomposites with 2.5% MCC/CNC concentration. Chitosan (Ch); Nanocrystalline Cellulose (CNC); Microcrystalline Cellulose (MCC).

Accessing the literature, it is known that chitosan powder has a characteristic broad peak close to $2\Theta = 20°$, related to the amorphous state (Mao et al., 2019; Patel et al., 2021; Wardhono et al., 2019). The lowering of this peak in the Ch film may be a sign that the original crystalline form of Ch was destroyed after mixing it with acetic acid.

Although the peaks continue to be visible, with the introduction of MCC/CNC in the polymer matrix, a decrease in the Ch characteristic peaks was observed. A slight increase in peak intensity was also observed at $2\Theta = 22.5°$, mainly for the film with 2.5% CNC commercial, indicating the successful blending of CNC and Ch. This peak is directly related to the crystallographic plane (200) present in crystalline cellulose I. The fact that it is possible to observe peaks referring to the two compounds that form the biocomposite is an indication of some preservation of the crystal structure of both. However, the gradual decrease mainly in the crystalline peak at $2\Theta = 11.4°$ in 2.5% MCC/CNC embedded films may assume that the nanoparticles slightly restricted the film crystallinity.

The incorporation of fillers modified the chitosan crystalline composition resulting in biocomposites with a higher crystalline index than the control sample film. The highest crystallinity index was registered by the film with 2.5% CNC Commercial, with 31.7%, and the lowest by the Ch control sample with 20.6%, as expected. Between the MCC/CNC samples was not verified significant differences in this index with values being around 23–25%.

4. Conclusion

This experimental work consisted mainly of two distinct parts. The first was biomass delignification and later the isolation of into micro and nanoparticles of cellulose. The initial stage was successfully achieved, resulting in fibers with about 90 % cellulose, which originated micro and nanocrystalline cellulose after acid hydrolysis. Both particles were then mixed and incorporated into chitosan films to act as reinforcement. The purpose was to produce functional material for packaging. The percentage of the MCC/CNC incorporated in the films did not affect the film homogeneity, color, and opacity. Regarding the mechanical, barrier, and thermal properties, meaningful differences were observed compared with the chitosan control film. Among the lignocellulosic biomasses, the MCC/CNC isolated from giant reed was the one that conferred the best properties to the Ch film, with 2.5% being considered the best amount tested. Further research is required to establish the ideal MCC/CNC concentrations. Additionally, the application of green solvents, like deep eutectic solvents or ionic liquids, to increase the process sustainability is intended to be done in future works, as well as the use of these biocomposites as layers for biodegradable packaging systems.

Declaration of Competing Interest

The authors declare that they have no known competing financial interests or personal relationships that could have appeared to influence the work reported in this paper.

Data Availability

Data will be made available on request.

Acknowledgements

This research was funded by national funding by FCT, Foundation for Science and Technology, MCTES, Portugal, through the individual PhD

research grant (SFRH/BD/144346/2019) of J.R.A.P. This work was also supported by the MEtRICs unit which is funded by national funds from FCT/MCTES (UIDB/04077/2020 and UIDP/04077/2020), by I3N-CENIMAT unit which is funded by FCT/MCTES (UIDB/50025/2020-2023) and by the Associate Laboratory for Green Chemistry - LAQV which is financed by national funds from FCT/MCTES (UIDB/50006/2020 and UIDP/50006/2020).

References

Akyuz, L., Kaya, M., Mujtaba, M., Ilk, S., Sargin, I., Salaberria, A.M., Labidi, J., Cakmak, Y.S., Islek, C., 2018. Supplementing capsaicin with chitosan-based films enhanced the anti-quorum sensing, antimicrobial, antioxidant, transparency, elasticity and hydrophobicity. Int. J. Biol. Macromol. 115, 438–446. https://doi.org/10.1016/j.ijbiomac.2018.04.040.

Alves, V.L.C.D., Rico, B.P.M., Cruz, R.M.S., Vicente, A.A., Khmelinskii, I., Vieira, M.C., 2018. Preparation and characterization of a chitosan film with grape seed extract-carvacrol microcapsules and its effect on the shelf-life of refrigerated Salmon (Salmo salar). LWT - Food Sci. Technol. 89, 525–534. https://doi.org/10.1016/j.lwt.2017.11.013.

ASTM International, 2018. ASTM D882-18. Standard Test Method for Tensile Properties of Thin Plastic Sheeting, West Conshohocken, PA.

Azeredo, H.M.C., Mattoso, L.H.C., Avena-Bustillos, R.J., Filho, G.C., Munford, M.L., Wood, D., McHugh, T.H., 2010. Nanocellulose reinforced chitosan composite films as affected by nanofiller loading and plasticizer content. J. Food Sci. 75, 1–7. https://doi.org/10.1111/j.1750-3841.2009.01386.x.

Barbosa, L.C. de A., 2007. Espectroscopia no infravermelho na caracterização de compostos orgânicos, 1a Edição. ed. Editora UFV.

Bernstein, P., Moholkar, V.S., 2020. Insight into chemical pretreatment of hardwood (Arundo donax) for improvement of pyrolysis. Bioresour. Technol. Rep. 11, 100545 https://doi.org/10.1016/j.biteb.2020.100545.

Bharimalla, A.K., Deshmukh, S.P., Vigneshwaran, N., Patil, P.G., Prasad, V., Deshmukh, S.P., Vigneshwaran, N., Patil, P.G., Prasad, V., 2017. Nanocellulose-polymer composites for applications in food packaging: current status, future prospects and challenges. Polym. Plast. Technol. Eng. 56, 805–823. https://doi.org/10.1080/03602559.2016.1233281.

Bhatnagar, P., Law, J.X., Ng, S.-F., 2021. Chitosan reinforced with kenaf nanocrystalline cellulose as an effective carrier for the delivery of platelet lysate in the acceleration of wound healing. Polym. (Basel) 13, 4392.

Brigham, C., 2018. Biopolymers: biodegradable alternatives to traditional plastics. Green Chemistry: An Inclusive Approach. Elsevier Inc,, pp. 753–770. https://doi.org/10.1016/B978-0-12-809270-5.00027-3.

Celebi, H., Kurt, A., 2015. Effects of processing on the properties of chitosan/cellulose nanocrystal films. Carbohydr. Polym. 133, 284–293. https://doi.org/10.1016/j.carbpol.2015.07.007.

Chakrabarty, A., Teramoto, Y., 2018. Recent advances in nanocellulose composites with polymers: A guide for choosing partners and how to incorporate them. Polymers 10, 517. https://doi.org/10.3390/polym10050517.

Chen, Y., Gan, L., Huang, J., Dufresne, A., 2019. Reinforcing mechanism of cellulose nanocrystals in nanocomposites. In: Huang, J., Dufresne, A., Lin, N. (Eds.), Nanocellulose: From Fundamentals to Advanced Materials. Wiley Online Library, pp. 201–249. https://doi.org/10.1002/9783527807437.ch7.

Collazo-Bigliardi, S., Ortega-Toro, R., Chiralt, A., 2018. Isolation and characterisation of microcrystalline cellulose and cellulose nanocrystals from co ff ee husk and comparative study with rice husk. Carbohydr. Polym. 191, 205–215. https://doi.org/10.1016/j.carbpol.2018.03.022.

Corsello, F.A., Bolla, P.A., Anbinder, P.S., Serradell, M.A., Amalvy, J.I., Peruzzo, P.J., 2017. Morphology and properties of neutralized chitosan-cellulose nanocrystals biocomposite films. Carbohydr. Polym. 156, 452–459. https://doi.org/10.1016/j.carbpol.2016.09.031.

Costa, S.M., Ferreira, D.P., Teixeira, P., Ballesteros, L.F., Teixeira, J.A., Fangueiro, R., 2021. Active natural-based films for food packaging applications: The combined effect of chitosan and nanocellulose. Int. J. Biol. Macromol. 177, 241–251. https://doi.org/10.1016/j.ijbiomac.2021.02.105.

Cumbane, B., Costa, J., Gussule, M., Gomes, L., Rodrigues, C., Souza, V.G.L., Fernando, A.L., 2020. Is the production of kenaf in heavy metal contaminated soils a sustainable option?. In: Wastes: Solutions, Treatments and Opportunities III - Selected papers from the 5th International Conference Wastes: Solutions, 2019 Treatments and Opportunities, pp. 512–517. https://doi.org/10.1201/9780429289798-81.

Ditzel, F.I., Prestes, E., Carvalho, B.M., Demiate, I.M., Pinheiro, L.A., 2017. Nanocrystalline cellulose extracted from pine wood and corncob. Carbohydr. Polym. 157, 1577–1585. https://doi.org/10.1016/j.carbpol.2016.11.036.

Dufresne, A., 2013. Nanocellulose: a new ageless bionanomaterial. Mater. Today 16, 220–227. https://doi.org/10.1016/j.mattod.2013.06.004.

El Achaby, M., El, N., Aboulkas, A., Zahouily, M., Bilal, E., Barakat, A., Solhy, A., 2017. Processing and properties of eco-friendly bio-nanocomposite films filled with cellulose nanocrystals from sugarcane bagasse. Int. J. Biol. Macromol. 96, 340–352. https://doi.org/10.1016/j.ijbiomac.2016.12.040.

Elias, N., Chandren, S., Attan, N., Mahat, N.A., Ilyana, F., Razak, A., Jamalis, J., Wahab, R.A., 2017. Structure and properties of oil palm-based nanocellulose reinforced chitosan nanocomposite for efficient synthesis of butyl butyrate. Carbohydr. Polym. 176, 281–292. https://doi.org/10.1016/j.carbpol.2017.08.097.

Emadian, S.M., Onay, T.T., Demirel, B., 2017. Biodegradation of bioplastics in natural environments. Waste Manag 59, 526–536. https://doi.org/10.1016/j.wasman.2016.10.006.

Fernando, A.L., Barbosa, B., Costa, J., Papazoglou, E.G., 2016. Giant reed (Arundo donax L.): a multipurpose crop bridging phytoremediation with sustainable Bioeconomy. Bioremediation and Bioeconomy. Elsevier Inc,. https://doi.org/10.1016/B978-0-12-802830-8.00004-6.

Fernando, A.L., Godovikova, V., Oliveira, J.F.S., 2004. Miscanthus x giganteus: contribution to a sustainable agriculture of a future/present – oriented biomaterial. Mater. Sci. Forum, Adv. Mater. Forum II 455–456, 437–441. https://doi.org/10.4028/www.scientific.net/msf.455-456.437.

Ferreira, A.R.V., Torres, C.A.V., Freitas, F., Sevrin, C., Grandfils, C., Reis, M.A.M., Alves, V.D., Coelhoso, I.M., 2016. Development and characterization of bilayer films of FucoPol and chitosan. Carbohydr. Polym. 147, 8–15. https://doi.org/10.1016/j.carbpol.2016.03.089.

Ferreira, F.V., Mariano, M., Rabelo, S.C., Gouveia, R.F., Lona, L.M.F., 2018. Isolation and surface modification of cellulose nanocrystals from sugarcane bagasse waste: From a micro- to a nano-scale view. Appl. Surf. Sci. 436, 1113–1122. https://doi.org/10.1016/j.apsusc.2017.12.137.

Fortunati, E., Luzi, F., Yang, W., Kenny, J.M., Torre, L., Puglia, D., 2018. Bio-based nanocomposites in food packaging. Nanomaterials for Food Packaging. Elsevier,, pp. 71–110. https://doi.org/10.1016/b978-0-323-51271-8.00004-8.

García, M.A., Rodríguez, M., Castro, C., De, N., 2020. Water vapor permeability of chitosan/zeolite composite films as affected by biopolymer and zeolite microparticle concentrations. J. Packag. Technol. Res. 4, 157–169. https://doi.org/10.1007/s41783-020-00092-y.

Gray, D.G., 2020. Cellulose nanocrystal research; A personal perspective. Carbohydr. Polym. 250, 116888 https://doi.org/10.1016/j.carbpol.2020.116888.

Higueras, L., López-carballo, G., Cerisuelo, J.P., Gavara, R., 2013. Preparation and characterization of chitosan/HP-β-cyclodextrins composites with high sorption capacity for carvacrol. Carbohydr. Polym. 97, 262–268. https://doi.org/10.1016/j.carbpol.2013.04.007.

Ismail, M.Y., Patanen, M., Antti, J., Visanko, M., Ohigashi, T., 2019. Hybrid films of cellulose nano fibrils, chitosan and nanosilica — Structural, thermal, optical, and mechanical properties. Carbohydr. Polym. 218, 87–94. https://doi.org/10.1016/j.carbpol.2019.04.065.

Izawa, H., Toyoshima, Y., Morimoto, M., Saimoto, H., Ifuku, S., 2021. Surface wrinkles induced on oriented chitosan films via horseradish peroxidase-catalyzed reaction and drying. Chem. Lett. 50, 252–255. https://doi.org/10.1246/cl.200740.

Karan, H., Funk, C., Grabert, M., Oey, M., Hankamer, B., 2019. Green bioplastics as part of a circular bioeconomy. Trends Plant Sci. 24, 237–249. https://doi.org/10.1016/j.tplants.2018.11.010.

Kargarzadeh, H., Ioelovich, M., Ahmad, I., Thomas, S., Dufresne, A., 2017. Methods for extraction of nanocellulose from various sources. Handbook of Nanocellulose and Cellulose Nanocomposites, Volume 1. Wiley Online Library,, pp. 1–49. https://doi.org/10.1002/9783527689972.

Karimi, S., Tahir, P., Dufresne, A., Karimi, A., Abdulkhani, A., 2014. A comparative study on characteristics of nanocellulose reinforced thermoplastic starch biofilms prepared with different techniques. Nord. Pulp Pap. Res. J. 29.

Khan, A., Khan, R.A., Salmieri, S., Le, C., Riedl, B., Bouchard, J., Tan, V., Kamal, M.R., Lacroix, M., 2012. Mechanical and barrier properties of nanocrystalline cellulose reinforced chitosan based nanocomposite films. Carbohydr. Polym. 90, 1601–1608. https://doi.org/10.1016/j.carbpol.2012.07.037.

Klemm, D., Cranston, E.D., Fischer, D., Gama, M., Kedzior, S.A., Kralisch, D., Kramer, F., Kondo, T., Lindström, T., Nietzsche, S., Petzold-welcke, K., Rauchfuß, F., Association, P.J., 2018. Nanocellulose as a natural source for groundbreaking applications in materials science: Today's state. Mater. Today 21, 720–748. https://doi.org/10.1016/j.mattod.2018.02.001.

Klochko, N.P., Barbash, V.A., Klepikova, K.S., Kopach, V.R., Tyukhov, I.I., Yashchenko, O.V., Zhadan, D.O., Petrushenko, S.I., Dukarov, S.V., Lyubov, V.M., Khrypunova, A.L., 2020. Use of biomass for a development of nanocellulose-based biodegradable flexible thin film thermoelectric material. Sol. Energy 201, 21–27. https://doi.org/10.1016/j.solener.2020.02.091.

Kumar, S., Mukherjee, A., Dutta, J., 2020. Chitosan based nanocomposite films and coatings: eEmerging antimicrobial food packaging alternatives. Trends Food Sci. Technol. 97, 196–209. https://doi.org/10.1016/j.tifs.2020.01.002.

Lv, W., Xia, Z., Song, Y., Wang, P., Liu, S., Zhang, Y., Ben, H., Han, G., Jiang, W., 2021. Using microwave assisted organic acid treatment to separate cellulose fiber and lignin from kenaf bast. Ind. Crop. Prod. 171, 113934 https://doi.org/10.1016/j.indcrop.2021.113934.

Mao, H., Wei, C., Gong, Y., Wang, S., Ding, W., 2019. Mechanical and water-resistant properties of eco-friendly chitosan membrane reinforced with cellulose nanocrystals. Polym. (Basel) 11, 166. https://doi.org/10.3390/polym11010166.

Martínez-Sanz, M., Erboz, E., Fontes, C., López-rubio, A., 2018a. Valorization of Arundo donax for the production of high performance lignocellulosic films. Carbohydr. Polym. 199, 276–285. https://doi.org/10.1016/j.carbpol.2018.07.029.

Martínez-Sanz, M., Erboz, E., Fontes, C., López-Rubio, A., 2018b. Valorization of Arundo donax for the production of high performance lignocellulosic films. Carbohydr. Polym. 199, 276–285. https://doi.org/10.1016/j.carbpol.2018.07.029.

Messa, L.L., Faez, R., 2020. Spray-dried chitosan/nanocellulose microparticles: synergistic effects for the sustained release of NPK fertilizer. Cellulose 27, 10077–10093. https://doi.org/10.1007/s10570-020-03482-2.

Mohaiyiddin, M.S., Ong, H.L., Othman, M.B.H., Julkapli, N.M., Villagracia, A.R.C., Akil, H.M., 2018. Swelling behavior and chemical stability of chitosan/nanocellulose biocomposites. Polym. Compos. 39, E561–E572. https://doi.org/10.1002/pc.24712.

Morais, J.P.S., Freitas, M.De, De, M., Souza, M.De, Dias, L., Magalhães, D., Ribeiro, A., 2013. Extraction and characterization of nanocellulose structures from raw cotton linter. Carbohydr. Polym. 91, 229–235. https://doi.org/10.1016/j.carbpol.2012.08.010.

Mujtaba, M., Salaberria, A.M., Andres, M.A., Kaya, M., Gunyakti, A., Labidi, J., 2017. Utilization of flax (Linum usitatissimum) cellulose nanocrystals as reinforcing material for chitosan films. Int. J. Biol. Macromol. 104, 944–952. https://doi.org/10.1016/j.ijbiomac.2017.06.127.

Ng, H., Sin, L.T., Bee, S., Tee, T., Rahmat, A.R., Sin, L.T., Bee, S., Tee, T., Rahmat, A.R., 2017. Review of nanocellulose polymer composite characteristics and challenges review of nanocellulose polymer composite characteristics and challenges. Polym. Plast. Technol. Eng. 56, 687–731. https://doi.org/10.1080/03602559.2016.1233277.

Noshirvani, N., Ghanbarzadeh, B., Rezaei, R., Hashemi, M., 2017. Novel active packaging based on carboxymethyl cellulose-chitosan -ZnO NPs nanocomposite for increasing the shelf life of bread. Food Packag. Shelf. Life 11, 106–114. https://doi.org/10.1016/j.fpsl.2017.01.010.

Pacáková, V., Virt, J., 2005. Plastics. In: Worsfold, P., Townshend, A., Poole, C. (Eds.), Encyclopedia of Analytical Science. Elsevier B.V, pp. 180–187. https://doi.org/10.1016/B0-12-369397-7/00467-2.

Patel, D.K., Dutta, S.D., Ganguly, K., Lim, K., 2021. Multifunctional bioactive chitosan/cellulose nanocrystal scaffolds eradicate bacterial growth and sustain drug delivery. Int. J. Biol. Macromol. 170, 178–188. https://doi.org/10.1016/j.ijbiomac.2020.12.145.

Pires, J., Paula, C.D.De, Gomes, V., Souza, L., Fernando, A.L., Coelhoso, I., 2021. Understanding the barrier and mechanical behavior of different nanofillers in chitosan films for food packaging. Polym. (Basel) 13, 721. https://doi.org/10.3390/polym13050721.

Pires, J.R.A., Gomes, L.A., Souza, V.G.L., Godinho, M.H., Fernando, A.L., 2022a. Evaluation and Comparison of Micro/Nanocellulose Extracted from Arundo, Kenaf and Miscanthus, 30th European Biomass Conference & Exhibition.

Pires, J., Souza, V., Fernando, A.L., 2019a. Valorization of energy crops as a source for nanocellulose production – current knowledge and future prospects. Ind. Crop. Prod. 140, 111642 https://doi.org/10.1016/j.indcrop.2019.111642.

Pires, J.R.A., Souza, V., Fernando, A.L., 2018. Chitosan/montmorillonite bionanocomposites incorporated with rosemary and ginger essential oil as packaging for fresh poultry meat. Food Packag. Shelf Life 17, 142–149. https://doi.org/10.1016/j.fpsl.2018.06.011.

Pires, J.R.A., Souza, V.G., Fernando, A.L., 2019b. Ecofriendly strategies for the production of nanocellulose from agro-industrial wastes. Eur. Biomass-.-. Conf. Exhib. Proc. 1781–1784.

Pires, J.R.A., Souza, V.G.L., Fuciños, P., Pastrana, L., Fernando, A.L., 2022b. Methodologies to assess the biodegradability of bio-based polymers — Current knowledge and existing gaps. Polym. (Basel) 14, 1359. https://doi.org/10.3390/polym14071359.

Rizzieri, R., Mahadevan, L., Vaziri, A., Donald, A., 2006. Superficial wrinkles in stretched, drying gelatin films. Langmuir 22, 3622–3626.

Salamon, D., 2014. Chapter 6 - Advanced Ceramics. In: Shen, J.Z., Kosmač, T. (Eds.), Advanced Ceramics for Dentistry. Elsevier B.V, pp. 103–122. https://doi.org/10.1016/C2011-0-07169-7.

Salari, M., Khiabani, M.S., Mokarram, R.R., Ghanbarzadeh, B., Kafil, H.S., 2018. Development and evaluation of chitosan based active nanocomposite films containing bacterial cellulose nanocrystals and silver nanoparticles. Food Hydrocoll. 84, 414–423. https://doi.org/10.1016/j.foodhyd.2018.05.037.

Shankar, S., Rhim, J., 2018. Bionanocomposite films for food packaging applications. Ref. Modul. Food Sci. 1–10. https://doi.org/10.1016/B978-0-08-100596-5.21875-1.

Soest, P.J.Van, 1963. Use of detergents in the analysis of fibrous feeds. 2. A rapid method for the determination of fiber and lignin. J. Assoc. . Agric. Chem. 46, 829–835.

Souza, V., Fernando, A.L., Pires, J.R.A., Freitas, P., Lopes, A.A.S., Braz, F.M., 2017. Physical properties of chitosan films incorporated with natural antioxidants. Ind. Crop. Prod. 107, 565–572. https://doi.org/10.1016/j.indcrop.2017.04.056.

Souza, V., Pires, J.R.A., Freitas, P., Lopes, A.A.S., Fernandes, F.M.B., Duarte, M.P., Coelhoso, I.M., Fernando, A.L., 2018. Bionanocomposites of chitosan/montmorillonite incorporated with Rosmarinus officinalis essential oil: development and physical characterization. Food Packag. Shelf Life 16, 148–156. https://doi.org/10.1016/j.fpsl.2018.03.009.

Souza, V., Pires, J.R.A., Rodrigues, C., Rodrigues, P.F., Silva, R.J., Caldeira, J., Duarte, M.P., Fernandes, F.B., Coelhoso, I.M., Fernando, A.L., 2019. Physical and morphological characterization of chitosan/montmorillonite films incorporated with ginger essential oil. Coatings 9, 700. https://doi.org/10.3390/coatings9110700.

Souza, V.G.L., Alves, M.M., Santos, C.F., Ribeiro, I.A.C., Rodrigues, C., Coelhoso, I., Fernando, A.L., 2021. Biodegradable chitosan films with ZnO nanoparticles and characterization. Coatings 11, 646.

Souza, V.G.L., Fernando, A.L., 2016. Nanoparticles in food packaging: biodegradability and potential migration to food-a review. Food Packag. Shelf Life 8, 63–70. https://doi.org/10.1016/j.fpsl.2016.04.001.

Sulaiman, S., Sahat, N.S., Omar, F.N., Noriznan, M., Naim, M.N., Baharuddin, A.S., Amran, M., 2020. Chemical-physical treatment for production of cellulose nanofiber from kenaf bast fiber. J. Nat. Fibers 1–12. https://doi.org/10.1080/15440478.2020.1863288.

Suranjoy, S., Lim, L., Manickavasagan, A., 2020. Ultrasound-assisted alkali-urea pre-treatment of Miscanthus × giganteus for enhanced extraction of cellulose fiber. Carbohydr. Polym. 247, 116758 https://doi.org/10.1016/j.carbpol.2020.116758.

Talebi, H., Ghasemi, F.A., Ashori, A., 2021. The effect of nanocellulose on mechanical and physical properties of chitosan-based biocomposites. J. Elastomers Plast. 1–20. https://doi.org/10.1177/00952443211017169.

Thakur, S., Chaudhary, J., Sharma, B., Verma, A., Tamulevicius, S., Thakur, V.K., 2018. Sustainability of bioplastics: opportunities and challenges. Curr. Opin. Green. Sustain. Chem. 13, 68–75. https://doi.org/10.1016/j.cogsc.2018.04.013.

Thomas, B., Raj, M.C., Athira, K.B., Rubiyah, M.H., Joy, J., Moores, A., Drisko, G.L., 2018. Nanocellulose, a versatile green platform: from biosources to materials and their applications. Chem. Rev. 118, 11575–11625. https://doi.org/10.1021/acs.chemrev.7b00627.

Tsalagkas, D., Borcsok, Z., Pasztory, Z., Gogate, P., Csoka, L., 2021. Assessment of the papermaking potential of processed Miscanthus × giganteus stalks using alkaline pre-treatment and hydrodynamic cavitation for delignification. Ultrason. Sonochem. 72, 105462.

Wang, Z., Yao, Z., Zhou, J., Zhang, Y., 2017. Reuse of waste cotton cloth for the extraction of cellulose. Carbohydr. Polym. 157, 945–952. https://doi.org/10.1016/j.carbpol.2016.10.044.

Wardhono, E.Y., Pinem, M.P., Kustiningsih, I., Agustina, S., Oudet, F., Lefebvre, C., Clausse, D., Saleh, K., Guénin, E., 2019. Cellulose nanocrystals to improve stability and functional properties of emulsified film based on chitosan nanoparticles and beeswax. Nanomaterials 9, 1–17.

Woranuch, S., Yoksan, R., 2013. Eugenol-loaded chitosan nanoparticles: I. Thermal stability improvement of eugenol through encapsulation. Carbohydr. Polym. 96, 578–585. https://doi.org/10.1016/j.carbpol.2012.08.117.

Xu, K., Liu, C., Kang, K., Zheng, Z., Wang, S., 2018b. Isolation of nanocrystalline cellulose from rice straw and preparation of its biocomposites with chitosan: physicochemical characterization and evaluation of interfacial compatibility. Compos. Sci. Technol. 154, 8–17. https://doi.org/10.1016/j.compscitech.2017.10.022.

Xu, D., Qin, H., Ren, D., 2018a. Prolonged preservation of tangerine fruits using chitosan/montmorillonite composite coating. Postharvest Biol. Technol. 143, 50–57. https://doi.org/10.1016/j.postharvbio.2018.04.013.

Yadav, M., Behera, K., Chang, Y.H., Chiu, F.C., 2020. Cellulose nanocrystal reinforced chitosan based UV barrier composite films for sustainable packaging. Polym. (Basel) 12. https://doi.org/10.3390/polym12010202.

Yang, J., Wang, X., Shen, B., Hu, Z., Xu, L., Yang, S., 2020. Lignin from energy plant (Arundo donax): pyrolysis kinetics, mechanism and pathway evaluation. Renew. Energy 161, 963–971. https://doi.org/10.1016/j.renene.2020.08.024.

Zarina, S., Ahmad, I., 2015. Biodegradable composite films based on κ-carrageenan reinforced by cellulose nanocrystal from kenaf fibers. BioResources 10, 256–271.

Zhang, X., Li, Y., Guo, M., Jin, T.Z., Arabi, S.A., He, Q., Ismail, B.B., Hu, Y., Liu, D., 2021. Antimicrobial and UV blocking properties of composite chitosan films with curcumin grafted cellulose nanofiber. Food Hydrocoll. 112, 106337 https://doi.org/10.1016/j.foodhyd.2020.106337.